Univerzita Karlova v Praze

Matematicko-fyzikální fakulta

BAKALÁŘSKÁ PRÁCE

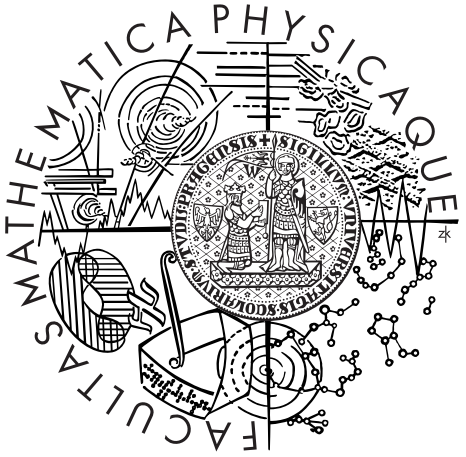

Pavol Štefko

Studium potlačení jetů ve srážkách těžkých iontů na LHC pomocí detektoru ATLAS

Ústav částicové a jaderné fyziky

Vedoucí bakalářské práce: Mgr. Martin Spousta, Ph.D.

Studijní program: Obecná fyzika

Praha 2013

Charles University in Prague

Faculty of Mathematics and Physics

BACHELOR THESIS

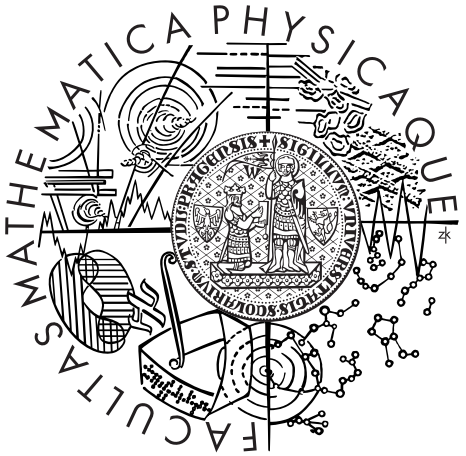

Pavol Štefko

Study of jet quenching in heavy ion collisions at LHC using ATLAS detector

Institute of Particle and Nuclear physics

Supervisor of the bachelor thesis: Mgr. Martin Spousta, Ph.D.

Study programme: General Physics

Prague 2013

Acknowledgments

I would like to express my deepest gratitude to my supervisor Mgr. Martin Spousta, Ph.D. and consultant Mgr. Martin Rybář for their leadership, patience and willingness. They offered invaluable assistance and guidance. Also, I would like to thank my parents for their unconditional love and support throughout my studies.

I declare that I carried out this bachelor thesis independently, and only with the cited sources, literature and other professional sources.

I understand that my work relates to the rights and obligations under the Act No. 121/2000 Coll., the Copyright Act, as amended, in particular the fact that the Charles University in Prague has the right to conclude a license agreement on the use of this work as a school work pursuant to Section 60 paragraph 1 of the Copyright Act.

In Prague, date 20.5.2013 signature of the author

Název práce: Studium potlačení jetů ve srážkách těžkých iontů na LHC pomocí detektoru ATLAS

Autor: Pavol Štefko

Katedra: Ústav částicové a jaderné fyziky

Vedoucí bakalářské práce: Mgr. Martin Spousta, Ph.D.

Abstrakt: Bola študovaná produkcia jetov v zrážkach jadier olova pri ťažiskovej energií na jeden nukleón 2,76 TeV použitím detektoru ATLAS na urýchľovači LHC. Predpokladá sa, že interakcie partónov s veľkou priečnou hybnosťou s horúcou, hustou hmotou produkovanou pri týchto ultrarelativistických kolíziách spôsobujú stratu energie produkovaných jetov (tzv. tlmenie jetov). Táto práca prezentuje výsledky analýzy jetov vykonanej na dátach získaných počas runu s ťažkými iónmi na LHC v roku 2011. Jety boli rekonštruované použitím anti-k_t algoritmu a študované ako funkcia centrality kolízie a dvojjetovej energetickej nerovnováhy. S rastúcou centralitou bol pozorovaný nárast asymetrie jetov, v súlade s teóriou tlmenia jetov. Ďalej potom štúdium dráh nabitých častíc indikuje nárast počtu častíc s malou priečnou hybnosťou v jete, ktorý podstúpil silné potlačenie.

Kľúčové slová: tlumenie jetov, zrážky ťažkých jadier, ATLAS, Veľký Hadrónový Urýchľovač

Title: Study of jet quenching in heavy ion collisions at LHC using ATLAS detector

Author: Pavol Štefko

Department: Institute of Particle and Nuclear physics

Supervisor: Mgr. Martin Spousta, Ph.D.

Abstract: Jet production in PbPb collisions at a per-nucleon center-of-mass energy of 2.76 TeV has been studied using the ATLAS detector at the LHC. Interactions between the high-p_{T} partons and the hot, dense medium, produced in these ultrarelativistic collisions, are expected to cause the loss of the jet energy (jet quenching). This thesis presents results of the jet analysis done on the data taken during the 2011 heavy-ion run at the LHC. Jets are reconstructed using the anti-k_t jet clustering algorithm and studied as a function of collision centrality and dijet energy imbalance. With increasing centrality, dijets are observed to be increasingly asymmetric, consistent with the theory of jet quenching. The study of charged particle tracks indicates the increase of the low-p_{T} tracks in the strongly quenched jets.

Keywords: jet quenching, heavy-ion collisions, ATLAS, Large Hadron Collider

Contents

Introduction

The subject of this thesis is a study of experimental measurements of jets in ultra-relativistic heavy-ion collisions and the phenomenon of jet quenching. Collisions of the heavy ions at these energies are expected to produce a dense medium of extremely high temperatures in order of trillion kelvins, as predicted from lattice quantum chromodynamics (QCD) calculations. This phase of matter consists of deconfined quarks and gluons as degrees of freedom and it is, therefore, accordingly called a quark-gluon plasma (QGP). QGP allows to test QCD in the limit of extreme temperatures and densities. What is also important, it is believed that the QGP existed at the very early stages of our universe. Therefore the study of the properties of this phase may provide a critical insight into the dynamics of this era.

Attempts to create and study the QGP have been previously made at CERN's (The European Organization for Nuclear Research) Super Proton Synchrotron (SPS) in the 1980s and 1990s, later at the Relativistic Heavy Ion Collider (RHIC) at the Brookhaven National Laboratory on Long Island (NY, USA) and most recently in PbPb collisions at CERN's Large Hadron Collider (LHC).

High transferred momentum interactions of quarks and gluons in colliding beams are known to produce highly collimated clusters of hadrons and other particles produced by hadronization referred to as jets. Jets have long been thought to interact with the ambient plasma and, therefore, to serve as probes of the QCD matter created in the collisions. The process by which a quark or gluon loses energy in a medium of high color charge density is called jet quenching.

Of special interest are the "dijets" consisting of the two energetic jets. These two jets are expected to have on average comparable energies and are also expected to be ejected in back-to-back geometry (i.e., having azimuthal difference close to π). However, the strong interactions of quarks and gluons inside the hot medium can significantly modify the dijet energy balance between the two most energetic jets. It is therefore important to study these modifications of dijet properties, since they can provide useful information about the properties of the QCD medium formed in the collisions.

The analysis in this work was made using the data from heavy-ion collisions at nucleon-nucleon center-of-mass energy 2.76 TeV, which were collected by the ATLAS (A Toroidal LHC ApparatuS) detector in 2011.

This thesis is organized as follows: Chapter 1 provides the theoretical background, introducing the main ideas of QGP and their consequences. These con-

cepts are developed in order to motivate the use of heavy-ion collisions as an experimental tool. Chapter 2 contains the descriptions of the experimental apparatuses, the ATLAS detector and the LHC, which provided the measurement data presented in this work. The results of the experimental analysis are presented in Chapter 3 with the conclusions following in the last chapter.

1 | Physical Background

1.1 The quark-gluon plasma

The quark-gluon plasma (QGP) is the main object of study in ultrarelativistic heavy ion physics. It is an unexplored state of matter in which the relevant degrees of freedom are not hadrons, but quarks and gluons. It is believed that the QGP is a primordial form of matter, which existed in the very early stages of our universe, for only few microseconds after the big bang [1].

1.1.1 General concepts of quantum chromodynamics

Quarks are one of the smallest known subdivisions of matter that have various intrinsic properties, including electric charge, color charge, mass, spin and flavor. They combine to form composite particles called hadrons, either baryons (consisting of three quarks) or mesons (consisting of one quark and one antiquark). The theory explaining the interactions among quarks is called the quantum chromodynamics (QCD).

Like in the quantum field theory describing the electromagnetism (EM), where the carriers of the EM force (gauge bosons) are photons, the interactions of QCD are realized by the exchanging of gluons, and the accompanying force is called the strong nuclear force. Quarks and gluons are collectively called *partons*. Quarks are the only known elementary particles in the standard model that engage in all four fundamental forces of contemporary physics (electromagnetism, gravitation, strong interaction, and weak interaction) [2].

One of the characteristic features of QCD is *color confinement*, often simply called confinement. This phenomenon explains the fact that no color charged particles (such as quarks or gluons) can ever be isolated and directly observed in our laboratories, because they are confined by the strong interaction. We can only observe particles carrying zero net color charge (e.g., baryons and mesons) [3]. The strong force favors confinement because at a certain range it is more energetically favorable to create a quark-antiquark pair than to continue to increase the distance between the quarks.

Another feature of QCD, closely related to that of confinement, is *asymptotic freedom*. This phenomenon was discovered in 1973 by David Gross and Frank Wilczek, and by David Politzer [4, 5]. It describes the behavior of quarks, which interact strongly at large distances (or small transverse momenta) and weakly at

small distances (or large transverse momenta). Under these conditions the QCD interactions are thought to be weak at high temperatures and densities, which can be achieved in heavy-ion collisions. Therefore, a new phase of matter called quark-gluon plasma may occur.

1.1.2 The QCD phase diagram

Phase diagrams are often used when physicists want to summarize the properties of matter over a range of various physical quantities. The control parameters in this case are temperature T and baryon chemical potential μ_B. The chemical potential can be intuitively thought of as a measure of net baryon density of the system [6]. In general, chemical potential describes the change of internal energy due to the change of the composition of the system (in our case, the number of baryons).

The phase diagram of quark matter is not very well known, both experimentally and theoretically. Fig. 1.1 shows the contemporary view of the QCD phase diagram. Each point on the diagram represents the state of thermodynamic equilibrium, characterized by the coordinates in $T \times \mu_B$ space. Phase coexistence lines are illustrated as solid blue lines, crossover region by dashed line. Filled circles represent critical points.

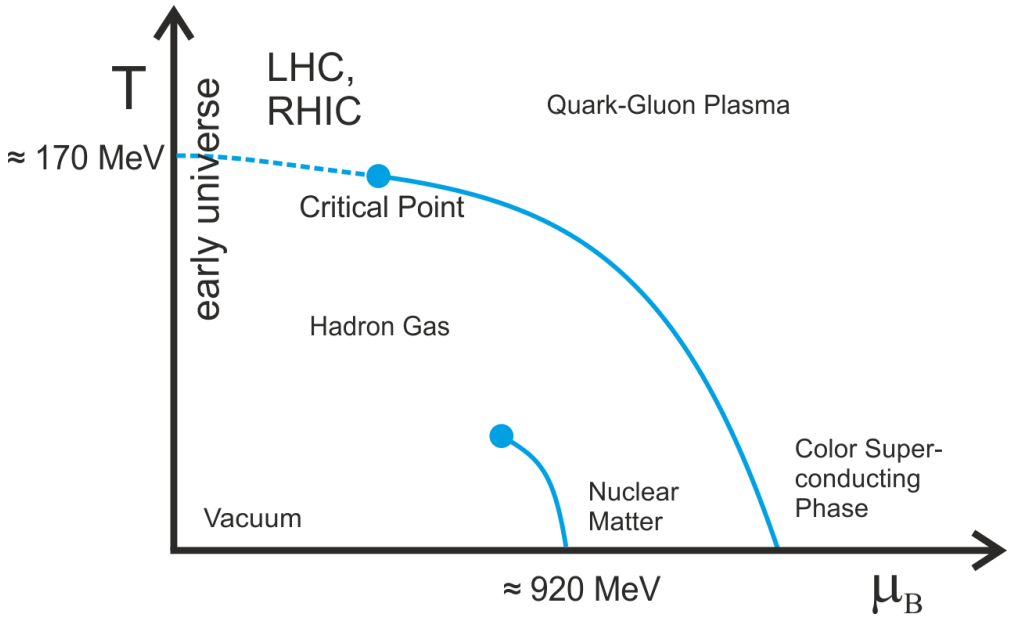

Figure 1.1: Schematic sketch of the QCD phase diagram showing the names of the various phases. For guidance it also shows the typical values of μ_B and T in heavy-ion collision experiments (LHC, RHIC) and in the early universe. Based on [8].

Let us now begin at the point in the vacuum where $T = \mu_B = 0$. As we move along the horizontal axis the temperature and the density are zero up to the point of $\mu_B \approx 920$ MeV where the density jumps to nuclear density. The process of crossing the coexistence lines is believed to be the *first-order phase transition*.

This process exhibits a discontinuity in the first derivative of the free energy with respect to pressure and temperature. Along the vertical axis, in the direction of increasing temperature, we go through the crossover region from hadron gas to the QGP. This is the area explored by ultrarelativistic heavy-ion colliders [7].

1.1.3 Heavy-ion collisions

The QGP can exist only in extreme conditions of very high energy densities and temperatures. In order to recreate matter at these conditions in the terrestrial laboratory, one collides heavy nuclei (heavy ions) at ultrarelativistic energies. Previous attempts to study the properties of the QGP created in heavy-ion collisions have been made at the Brookhaven National Laboratory on Long Island (NY, USA) at the Relativistic Heavy Ion Collider (RHIC), which was the world's highest energy accelerator of heavy ions before the launch of the Large Hadron Collider (LHC) in 2008 [9]. Further details about the LHC machine will be discussed in Chapter 2.

In center-of-mass frame, as they fly towards each other, the colliding nuclei appear as two Lorenz-contracted discs. It is expected that during the collision, the nuclei deposit a large amount of energy into a very small volume in the collision region. As estimated by Bjorken [10], the energy density can be so high that these reactions might provide the conditions for the creation of the QGP.

The most frequent events at low energy nuclear physics ($\sqrt{s_{\mathrm{NN}}} \approx 1$ MeV) are elastic collisions and low energy inelastic collisions. In both cases the final multiplicity (the number of particles after the reaction) is quite small. However, the multiplicities in (ultra)relativistic heavy-ion collisions[1] are very large. The number of produced particles may exceed 1000, which is much more than the number of initial nucleons [11].

This leads to special experimental requirements. For example the track recognition problem becomes very difficult at large multiplicities. It is also advantageous if we can detect all of the created particles in an event. Because of this, it is desired for the detector to cover full 2π in azimuth. As we will see, these conditions are partially fulfilled by the ATLAS detector at LHC (see Sec. 2.2).

Moreover, the energy frontier achieved at LHC provides us with the tool to study the interactions inside this medium. This tool is known as *jet quenching*.

1.2 Jets as the QGP probes

Let us first consider a collision of simple "QCD systems", for example two protons[2]. During a large-momentum-transfer scattering processes in high-energy collisions, as the original quarks inside the protons separate, the energy of the strong

[1] The energy region of ultrarelativistic heavy ion reactions starts at around 10 GeV center-of-mass energy.

[2] We call these systems simple because, as opposed to the much more complex systems encountered in heavy-ion collisions, only few of the partons interact.

nuclear field between them increases up to the point when there is enough energy to create a new quark-antiquark pairs [12]. Due to postulated confinement, the quarks escaping from the collision cannot exist individually. Instead, free quarks created in collision combine with quarks and antiquarks created spontaneously from the vacuum to form hadrons [13]. This process is called *hadronization* and leaves us with two sets of hadrons travelling in the opposite directions. They are usually collimated in two cones around the direction of the two original partons and we refer to them as *jets*. Schematic picture of the jet production in proton-proton (pp) and lead-lead (PbPb) collision is shown in Fig. 1.2.

Since we cannot measure the original parton, jet has to be defined by a jet finding algorithm. It is a set of rules that postulate how to cluster the products of the hadronization into an object whose kinematics is as close as possible to the kinematics of the original parton.

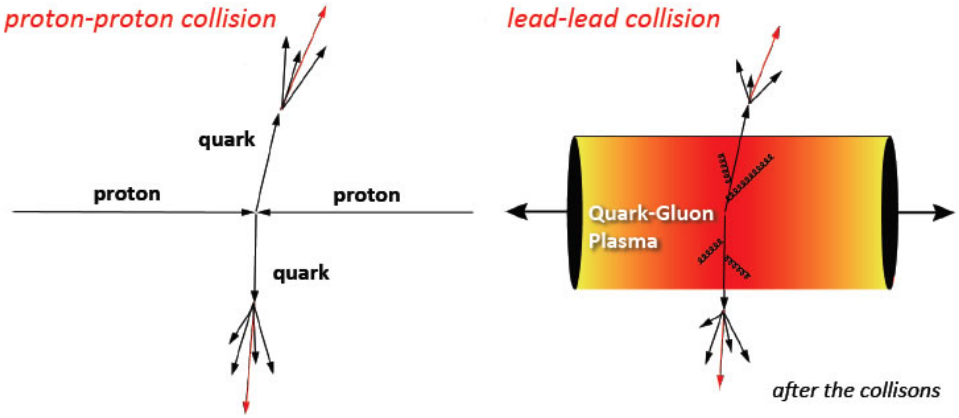

Figure 1.2: Sketch of a hard scattering, showing the jet production in proton-proton (left) and lead-lead (right) collisions. The colliding nuclei in the right picture are displayed as thin discs due to the Lorenz contraction. Note that the jets created in heavy-ion collision are modified due to the interactions of quarks with the QGP. Ref. [14].

One of the main differences between proton-proton collisions and heavy-ion collisions is the presence of the QGP in the latter. In these conditions the products of the potential scattering processes interact heavily with the ambient plasma, experiencing collisional and radiative energy loss, via scattering and gluon bremsstrahlung ("gluonstrahlung"), respectively [15, 16]. It is expected that the radiative energy loss dominates over collisional energy loss. The amount of energy loss is predicted to be proportional to the energy density of the medium. Hence jets, which have lost significant amount of energy while propagating through the medium, can be used as probes of the medium, providing information about its structure and properties [16]. In this way jets play a distinct role in ultrarelativistic heavy-ion physics.

Bjorken was the first one who recognized the potential of jets as a tool to study the QGP. He suggested that high energy quarks and gluons suffer differential energy loss while propagating through the plasma [10]. He also pointed out the

extreme case when the hard collision occurs at the periphery of the hot medium resulting in one jet being almost unquenched, and the other jet being totally absorbed. An example of such an asymmetric event measured by the ATLAS experiment is illustrated in Fig. 1.3.

On the left, a view along the beam axis is pictured with high-p_{T} charged particle tracks indicated by the lines and energy responses in calorimeters by colored bars. The middle figure shows the E_{T} distribution in $\eta \times \phi$ space. On the right a similar distribution is shown for the charged particle tracks in the Inner Detector. It is consistent with the calorimeter signal[3].

Jet quenching, or high-p_{T} parton suppression, has already been observed in the collisions of golden nuclei at RHIC [17], but the LHC heavy-ion program allows us to study this phenomenon at much higher energies than previously achieved at RHIC and, therefore, to use fully reconstructed jets [18].

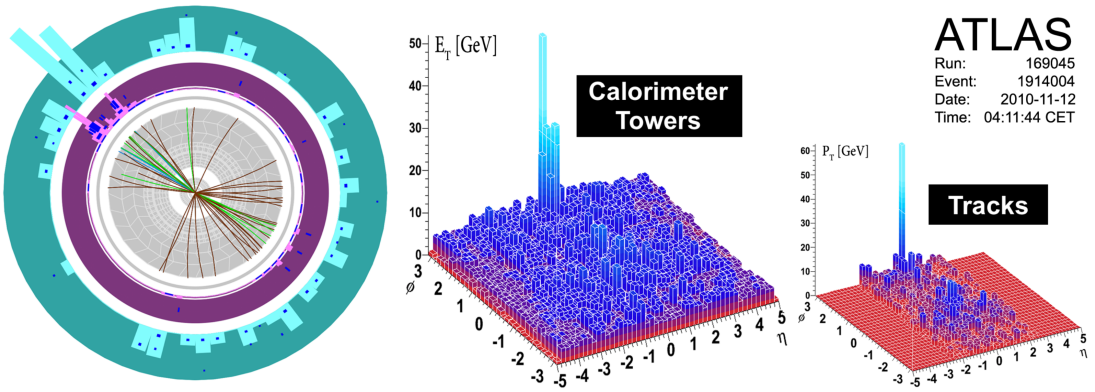

Figure 1.3: Event display of a highly asymmetric dijet event, recorded by ATLAS during the early portion of the 2010 PbPb run, with one highly energetic jet and no visible recoiling jet. Ref. [18].

[3]Mentioned physical quantities and experimental apparatus are further discussed in section 2.2

2 | Experimental Setup

2.1 The Large Hadron Collider

The Large Hadron Collider (LHC) is a particle accelerator and collider located at CERN outside Geneva, Switzerland. It was primarily constructed to collide protons, however, the machine is also capable of colliding heavy ions. The first lead ion collisions took place in November 2010.

The LHC machine[1] is installed in the tunnel which was originally constructed for LEP (Large Electron–Positron Collider). The tunnel itself has 26.7 km in diameter and contains eight arcs and eight straight sections. It lies between 45 m and 170 m under the ground on the borders of Switzerland and France. By contrast to the particle-antiparticle colliders, the LHC accelerator is designed to collide particles with the same charge sign. For this reason it has two parallel rings with counter-rotating beams. Figure 2.1 shows the location of the LHC tunnel, and the location of the four large experiments around its ring.

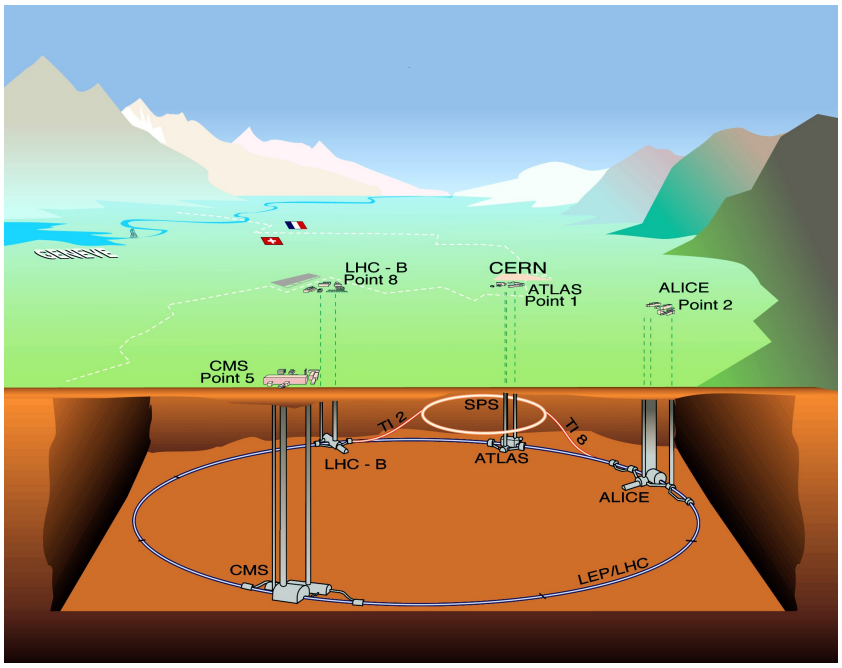

Figure 2.1: Overall view of the LHC and its 4 main experiments. Ref. [21].

[1]If not stated otherwise, all information about the LHC were taken from the LHC design paper [19].

As previously mentioned, the LHC main physics program is based on proton-proton (pp) collisions. However, typically one month per year, runs with heavy-ion ($^{208}Pb^{82+}$) collisions are included. The LHC injector chain for Pb ions is almost identical to the one for protons. The ions go from source through a series of linear and circular accelerators before entering the LHC. The first of them is a linear accelerator Linac 3, after that the ions go through three circular accelerators, namely the Low Energy Ion Ring (LEIR), the Proton Synchrotron (PS) and the Super Proton Synchrotron (SPS). This sequence is also schematically shown in Fig. 2.2.

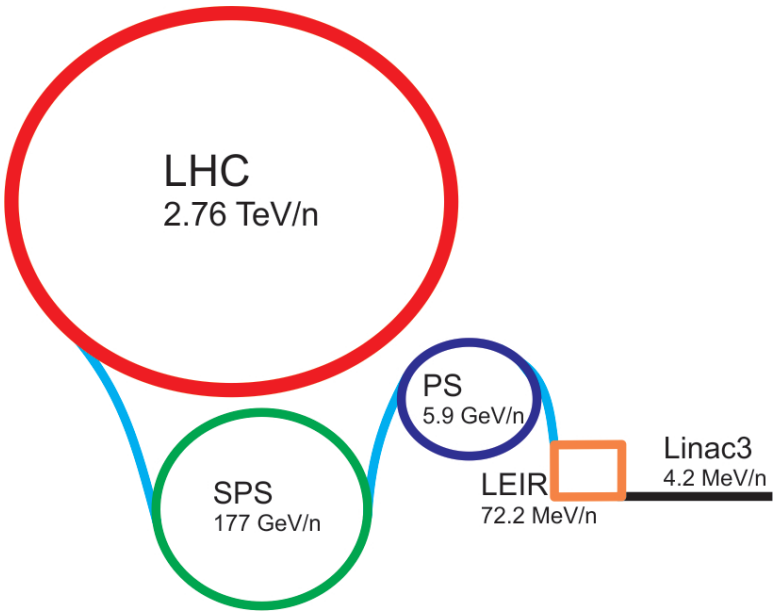

Figure 2.2: Scheme of the LHC ion injection chain with corresponding output energies per nucleus taken from [20].

The Pb^{27+} ions extracted from source need to be fully stripped from electrons before entering the LHC. This is assured by two aluminium foil strippers. The first one is located in Linac3 and provides the conversion to Pb^{54+}. The second stripping occurs in the line between PS and SPS. After extraction from PS the Pb beam is fully stripped by a 0.8 mm aluminium foil [20].

2.2 The ATLAS Experiment

ATLAS[2] (A Toroidal LHC ApparatuS) is one of the seven particle detectors at the LHC and together with the CMS (Compact Muon Solenoid) one of two general purpose detectors. It is built at interaction point 1 (IP1) of the LHC ring and is capable of studying both pp and PbPb collisions at unprecedented luminosity. Its massive dimensions are 44 m in length, 25 m in height and it weighs about 7000 tons. The illustration on Fig. 2.3 provides overall cut-away view of the ATLAS detector.

[2]If not stated otherwise, all information about the ATLAS detector were taken from [22].

Following sections are devoted to the more detailed description of this experiment. In Section 2.2.1 we will define several concepts and physical quantities which are often used in accelerator physics. This Section also defines the coordinate system generally used in the ATLAS experiment. The Section 2.2.2 then describes various parts and sub-detectors of ATLAS.

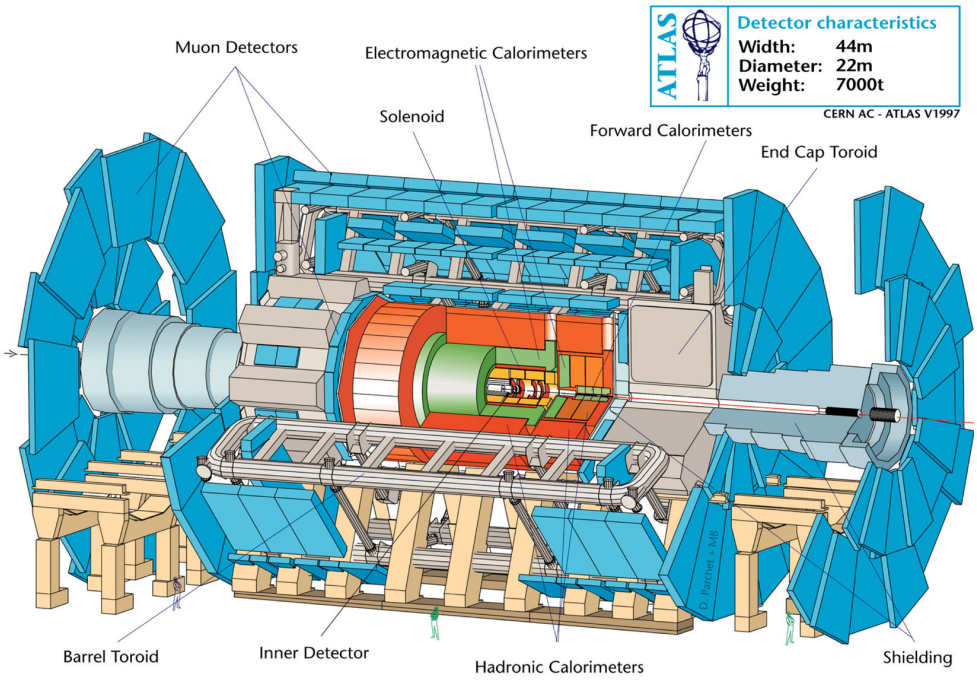

Figure 2.3: Cut-away view of the ATLAS detector highlighting various parts of the experiment [23].

2.2.1 The ATLAS coordinate system and related concepts

The origin of the ATLAS coordinate system is located in the nominal interaction point. The z-axis is defined by the beam direction while the x-y plane is perpendicular to the beam direction. The positive x-axis points towards the center of the LHC tunnel and the positive y-axis is defined as pointing upwards. The orientation of the z-axis therefore follows from the right-handedness of the coordinate system.

The azimuthal angle ϕ is measured as the angle in the x-y plane. The $\phi = 0$ corresponds to the positive x-axis and increases clock-wise looking in the positive z direction. The polar angle ϑ is measured as the angle from the positive z-axis. By definition, ϑ is 0 or π along the beam axis and $\pi/2$ on the transverse plane.

Considering a particle with momentum vector $\mathbf{p} = (p_x, p_y, p_z)$ and energy E experimental particle physicists often use *rapidity* y as an alternative to speed as a measure of motion. It is defined as [24]:

$$y = \frac{1}{2} \ln \left(\frac{E + p_z}{E - p_z} \right). \tag{2.1}$$

Rapidity is not Lorentz-invariant, it is, however, additive under the boosts along the z-axis. For $p \gg m$ or, equivalently, $m/p \to 0$ the Eq. (2.1) can be expanded and simplified to obtain the definition of *pseudorapidity*:

$$\eta = -\ln\left(\tan\left(\frac{\vartheta}{2}\right)\right). \tag{2.2}$$

This quantity gives us only geometric information about the direction of the particle and does not require the knowledge of mass of the particle. Unlike rapidity, pseudorapidity is not additive under longitudinal boosts.

We define the *transverse momentum* p_{T} as the projection of the momentum vector on the x-y plane:

$$p_{\mathrm{T}} = |\mathbf{p}| \sin\vartheta = \sqrt{p_x^2 + p_y^2}. \tag{2.3}$$

The *transverse energy* of a particle is defined as its energy in the rest frame where its $p_z = 0$. We can write[3] [25]:

$$E_{\mathrm{T}} = E \sin\vartheta = \sqrt{m^2 + p_{\mathrm{T}}^2}, \tag{2.4}$$

where m is the rest (invariant) mass of the particle.

Azimuthal angle ϕ, pseudorapidity η, E_{T} and p_{T} are four quantities that can fully characterize the particle. We can therefore say that E_{T} and p_{T} are measured in $\eta \times \phi$ space.

A total energy accessible in the collision is quantified by the *center-of-mass energy*, which can be expressed in the Lorentz invariant form[4] [24]:

$$\sqrt{s} = \sqrt{(p_1 + p_2)^2} = \sqrt{(E_1 + E_2)^2 - (\mathbf{p_1} + \mathbf{p_2})^2}, \tag{2.5}$$

where p_1 and p_2 are the four-momenta of the incoming particles.

In heavy-ion collisions, it is common to use the energy per nucleon-nucleon pair $\sqrt{s_{\mathrm{NN}}}$. Typical values of $\sqrt{s_{\mathrm{NN}}}$ for AuAu collisions at RHIC have been 130 GeV [26] and 200 GeV [17]. The LHC currently operates at 2.76 TeV per-nucleon center-of-mass energy and it is planned to reach $\sqrt{s_{\mathrm{NN}}} = 5.5$ TeV, which corresponds to designed 7 TeV for protons.

An important factor in a collider run is the *luminosity*. The beams in today's colliders consist of bunches of ions. If two bunches containing n_1 and n_2 particles collide head-on with frequency f, the *instantaneous luminosity*, $\mathscr{L}$, of a beam can be expressed as:

$$\mathscr{L} = f\frac{n_1 n_2}{4\pi\sigma_x\sigma_y}, \tag{2.6}$$

where σ_x and σ_y characterize the transverse beam profiles in the horizontal and

[3] Using the convention where $c = 1$.

[4] This formula takes into consideration the collision of two particles with the energies E_1 and E_2 and momenta vectors $\mathbf{p_1}$ and $\mathbf{p_2}$. The square of the momenta therefore plays the role of the dot product.

vertical directions. It is assumed that the transverse profiles of the colliding bunches are identical and that the profiles are independent of position along the bunch.

The integral over time of the instantaneous luminosity is the *integrated luminosity*. It is used to calculate the number of events N with cross section σ:

$$N = \sigma \int \mathscr{L}(t)\mathrm{d}t. \tag{2.7}$$

Luminosity is clasically stated in units of $\mathrm{cm}^{-2}\mathrm{s}^{-1}$. Integrated luminosity, on the other hand, is usually quoted as the inverse of the standard measures of cross section, such as barns [24].

This thesis focuses on the phenomenon of jet quenching. It is therefore useful to define two more quantities regarding jets. One of them is the *jet axis* which characterizes the jet position in $\eta \times \phi$ phase space and gives us information about the direction of the parton from which the jet originates. It can be defined e.g., as a transverse energy weighted position of constituents of jets:

$$\phi_{\mathrm{jet}} = \frac{\sum\limits_{i\in\mathrm{jet}} E_{\mathrm{T},i}\phi_i}{\sum\limits_{i\in\mathrm{jet}} E_{\mathrm{T},i}}, \qquad \eta_{\mathrm{jet}} = \frac{\sum\limits_{i\in\mathrm{jet}} E_{\mathrm{T},i}\eta_i}{\sum\limits_{i\in\mathrm{jet}} E_{\mathrm{T},i}}, \tag{2.8}$$

where η_i, ϕ_i and $E_{\mathrm{T},i}$ are the position in $\eta \times \phi$ space and transverse energy of constituents of jets. Constituents of jets are particles or calorimeter cells that are assigned to a jet by the jet finding algorithm mentioned in Section 1.2. Each jet finding algorithm has a distance parameter, or *radius*, R, which is the area in $\eta \times \phi$ space that is covered by a jet.

2.2.2 The sub-detectors

The ATLAS detector is forward-backward symmetric with respect to the interaction point and covers almost the full 2π in azimuth. It consists of four main subdetector systems [23].

- **The Inner Detector (ID):** This is the innermost sub-detector beginning only 50 millimeters from the beam axis. It has a cylindrical shape with a length of 7 m and the outer radius of 1.15 m. These dimensions cover a pseudorapidity region of $|\eta| < 2.5$. Its main purpose is the tracking of the charged particles and measuring their momentum. It is also capable of reconstructing the primary interaction vertex and particle decay vertices. Fig. 2.4 contains the illustration of this sub-detector.

  The ID is immersed in the solenoidal magnetic field of 2 T which curves the tracks of charged particles allowing the momentum measurements. The detector is composed of three independent sub-detectors. These are (in order of increasing radius): silicon pixel detector, a silicon microstrip detector (SCT) and, finally, a straw tube transition radiation tracker (TRT).

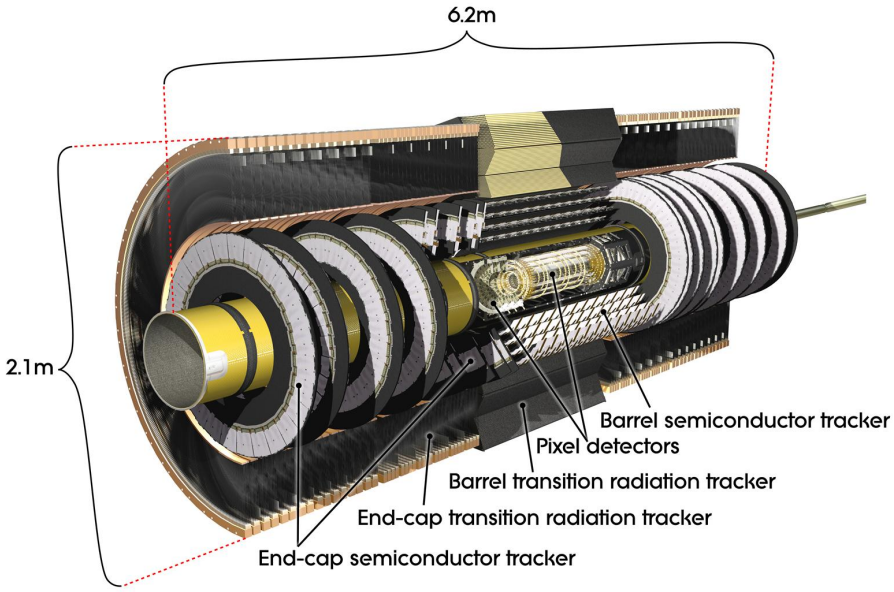

Figure 2.4: Overall view of the Inner Detector [23].

- **The Calorimeter System:** The ATLAS calorimeters are designed to stop the particles through the electromagnetic and strong interactions. This system is composed of electromagnetic (EM) and hadronic calorimeters, each using a different technology to measure the energy of particles. Liquid argon technology (LAr) is used by the EM calorimeters (and some hadronic calorimeters) and scintillation tiles by the hadronic ones. The fine segmentation of both types of calorimeters is well-suited for measuring jets [18].

  When the particle strikes an absorber (thick metal layer) it initiates EM and/or hadronic showers. The energy of the incident particle is spread among the lower energy particles in the cascade. Behind the absorber is placed an active material which collects some of the energy of these particles, either through ionization (LAr) or scintillation (tiles). Alternating layers of absorber and active material are placed in succession and the shower-sampling is repeated. As a consequence, the energy of the particle can be determined.

  In order to limit punch-through of the particles into the muon system the thickness of the calorimeters is an important parameter. Moreover, the absorbing material is chosen to be dense in order to absorb the particles. Figure 2.5 highlights various parts of the ATLAS calorimetric system. The EM calorimeter covers the pseudorapidity range of $|\eta| < 3.2$. The hadronic calorimetry which uses the steel and scintillating tiles covers the range of $|\eta| < 1.7$. LAr technology is also used in hadronic end-cap calorimeters covering the range of $1.5 < |\eta| < 3.2$. Finally, the LAr forward calorimeters (FCal) extend the pseudorapidity coverage up to $|\eta| = 4.9$. As we will see in section 3.2.1 the FCal system plays a special role in the ATLAS heavy-ion analyses.

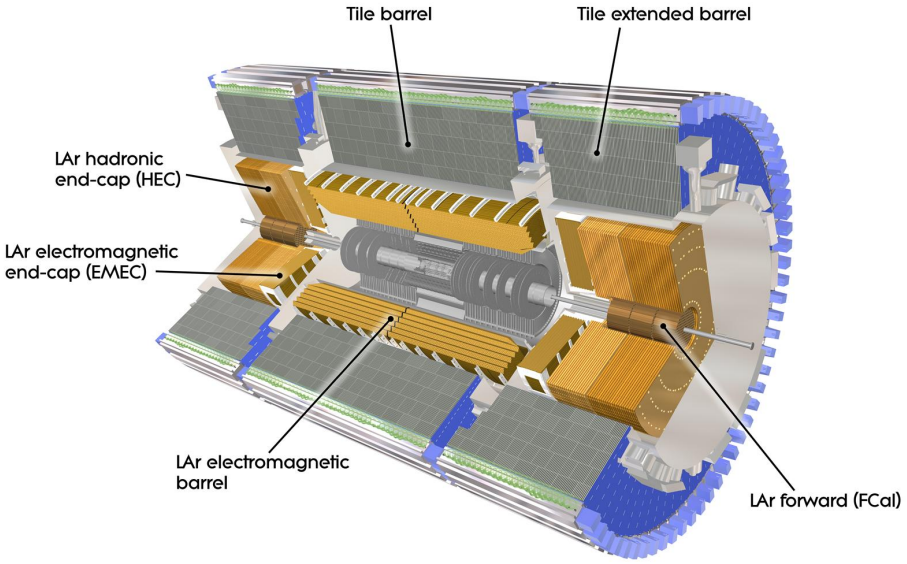

Figure 2.5: Cut-away view of the ATLAS calorimeters [23].

- **The Muon Spectrometer:** Figure 2.6 shows the layout of the muon spectrometer. This system is located on the outermost part of the detec-

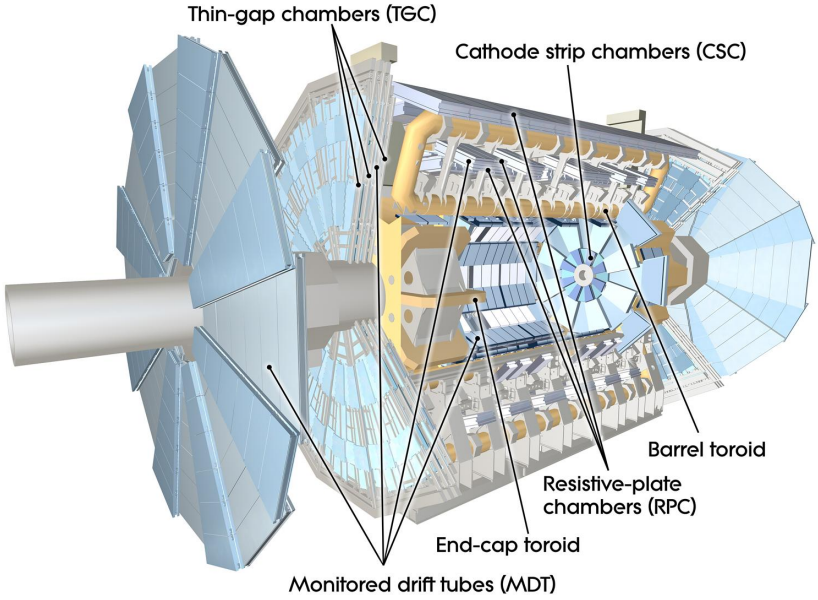

Figure 2.6: Layout of the muon spectrometer [23].

tor (see Fig. 2.3) because the muons with sufficient energy are the only detectable particles that can pass the calorimetric system without being stopped. It consists of monitored drift tubes (MDTs) for precision tracking in the spectrometer, Resistive Plate Chambers (RPCs) and Thin Gap Chambers (TGCs) for triggering in barrel and endcap, respectively, and Cathode Strip Chambers (CSCs) for detailed measurements in the high-rate endcap inner layer where MDTs would have occupancy problems. Like

in the ID the momenta of muons are measured using a magnetic field provided by the magnets described in the following paragraph.

- **The Magnet System:** The main purpose of this system is, as previously mentioned, bending the tracks of the charged particles for precise momentum measurements. It consists of the magnets used in the ID and the muon spectrometer. The system of magnets for the latter consists of large barrel toroid for $|\eta| < 1.4$, two smaller end-cap magnets for the range $1.6 < |\eta| < 2.7$ and by the combination of the two in the transit region $(1.4 < |\eta| < 1.6)$.

3 | Experimental Analysis

3.1 Definition and general behavior of the missing p_{T}

The law of conservation of momentum dictates that the total sum of transverse momenta vectors $\mathbf{p}_{\mathrm{T}}$ of all the particles created in the collision should be zero[1]:

$$\mathbf{p}_{\mathrm{T}} = \sum_{i=0}^{N} \mathbf{p}_{\mathrm{T},i} = \mathbf{0}, \tag{3.1}$$

where i is the integer labeling the particle and N is the total number of particles produced in the collision (i.e., the multiplicity of the collision). In other words, the $\mathbf{p}_{\mathrm{T}}$ vector calculated by adding the $\mathbf{p}_{\mathrm{T},i}$ vectors of individual particles produced in an event should be a zero vector.

This fact is, however, almost never observed in real experiments. We can, therefore, talk about a *missing transverse momentum vector* $\not{\mathbf{p}}_{\mathrm{T}}$. This observable is of high importance when studying the phenomenon of jet quenching. It is usually calculated by adding the momenta vectors of all reconstructed ID tracks present in an event vectorially and multiplying this by -1, as defined in the following equation:

$$\not{\mathbf{p}}_{\mathrm{T}} \equiv -\sum_{i=0}^{N} \mathbf{p}_{\mathrm{T},i} = -\mathbf{p}_{\mathrm{T}}. \tag{3.2}$$

A nonzero $\not{\mathbf{p}}_{\mathrm{T}}$ in an event usually has contributions from many sources. The primary source of missing p_{T} are neutrinos, which are produced in weak interactions and which escape from typical collider detectors without producing any direct response in the detector elements. The presence of such particles must be deduced from the overall imbalance of the total momentum [27]. Another contributions to $\not{\mathbf{p}}_{\mathrm{T}}$ include measurement resolution, instrumental defects in the detector system and reconstruction inefficiencies. Apart from the undetected particles, these contributions are considered unwanted, because they distort the measurements.

[1]The summation sign here denotes the vector sum.

3.1.1 Toy Monte Carlo

Before we started the analysis of the real data taken by ATLAS a simple Monte Carlo (MC) simulation has been performed. The main purpose of this simulation was to define $\not{\mathbf{p}}_{\mathrm{T}}$ and to study the main properties of this quantity under idealized conditions. Moreover, it served as a simple learning tool, which introduced the author of this work into the world of particle physics data analysis using the ROOT framework [28].

This MC was based on random number generation. It created a set of N_{C} virtual collisions, each with a different number of particles. The amount of particles in each collision was uniformly distributed from $N_{\mathrm{p,min}}$ to $N_{\mathrm{p,max}}$. Every particle in an event was assigned a value of $p_{\mathrm{T},i}$[2] and an azimuthal angle ϕ_i. The values of ϕ_i were uniformly distributed over the interval $[-\pi, \pi]$ and the number of particles N carrying the transverse momentum p_{T}, $N(p_{\mathrm{T}})$, followed the exponential distribution:

$$N(p_{\mathrm{T}}) = ae^{-b \cdot p_{\mathrm{T}}},$$

where a and b are free parameters chosen to be 1 and 5, respectively. Note that the behavior of quantities discussed further (especially of $\not{p}_{\mathrm{T}}$) does not depend on the choice of these parameters.

From the value of $p_{\mathrm{T},i}$ and corresponding angle ϕ_i we calculated the x and y components of the transverse momentum of a given particle i using simple formulae:

$$p^{\mathrm{x}}_{\mathrm{T},i} = p_{\mathrm{T},i} \cdot \cos\phi_i, \tag{3.3}$$

$$p^{\mathrm{y}}_{\mathrm{T},i} = p_{\mathrm{T},i} \cdot \sin\phi_i. \tag{3.4}$$

For every event the values of $p^{\mathrm{x}}_{\mathrm{T}}$ and $p^{\mathrm{y}}_{\mathrm{T}}$ of every particle were summed to obtain the final vector $\mathbf{p}_{\mathrm{T}}$. The magnitude of this vector reads as:

$$p_{\mathrm{T}} = \sqrt{\left(\sum_i p^{\mathrm{x}}_{\mathrm{T},i}\right)^2 + \left(\sum_i p^{\mathrm{y}}_{\mathrm{T},i}\right)^2}. \tag{3.5}$$

The vector $\not{\mathbf{p}}_{\mathrm{T}}$ is, according to the Eq. (3.2), just the vector of $\mathbf{p}_{\mathrm{T}}$ with the minus sign. Thus they both have equal magnitude.

The individual x and y components of $\not{\mathbf{p}}_{\mathrm{T}}$ can, therefore, be calculated as:

$$\not{p}^{\mathrm{x}}_{\mathrm{T}} = -\sum_i p^{\mathrm{x}}_{\mathrm{T},i}, \tag{3.6}$$

$$\not{p}^{\mathrm{y}}_{\mathrm{T}} = -\sum_i p^{\mathrm{y}}_{\mathrm{T},i}. \tag{3.7}$$

These are the quantities we will thoroughly discuss throughout the rest of the text.

[2] If the sign for the vectorial quantity is not in boldface it denotes the magnitude of the vector.

The values of parameters used in this simulation were: $N_{\mathrm{C}} = 100,000$; $N_{\mathrm{p,min}} = 10$ and $N_{\mathrm{p,max}} = 6,000$. Each event was assigned to one of six bins according to the number of particles in the event, that is, according to the "activity" of the collision. In real collisions the activity of the event reflects the centrality of the collision, which is a crucial quantity in the heavy-ion physics and which is further discussed in Sec. 3.2.1.

The distribution of $\not{p}_{\mathrm{T}}$ for each of these bins is displayed in Fig. 3.1. This plot does not have an associated unit for the $\not{p}_{\mathrm{T}}$, because we are only interested in the qualitative behavior of the distribution. Histograms are normalized according to the number of entries in each activity bin[3].

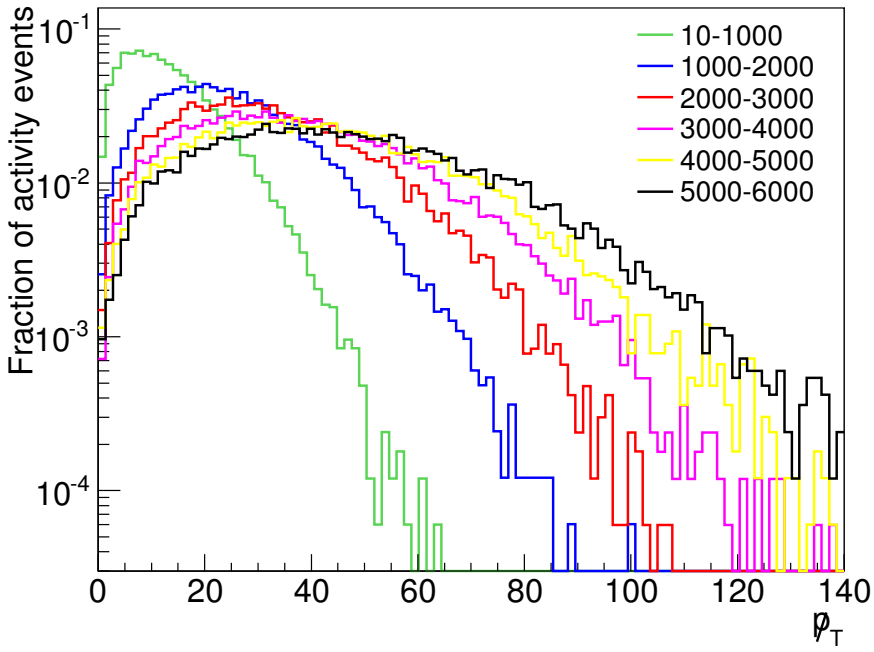

Figure 3.1: Probability distribution of $\not{p}_{\mathrm{T}}$ for six activity bins in MC simulation.

Let us now introduce one more quantity regarding $\not{p}_{\mathrm{T}}$, the *missing* p_{T} *significance* $\not{p}_{\mathrm{T}}^{\mathrm{sign}}$, which shall help us to understand the behavior of missing p_{T}. It is defined for each collision as $\not{p}_{\mathrm{T}}$ divided by the square root of the total transverse momentum of all the particles in that collision:

$$\not{p}_{\mathrm{T}}^{\mathrm{sign}} = \frac{\not{p}_{\mathrm{T}}}{\sqrt{\sum_i p_{\mathrm{T},i}}}. \tag{3.8}$$

In an idealized case of our MC simulation, the distribution of $\not{p}_{\mathrm{T}}^{\mathrm{sign}}$ should be the same for each centrality bin (as explained later). This is really the case, as shown in Fig. 3.2. The reason for this will be explained further.

Looking at the Figures 3.1 and 3.2, one could wonder about the origin of the $\not{p}_{\mathrm{T}}$. Remember that this is just a very simple MC simulation, without any im-

[3]Note that the rest of the histograms in this work shall be normalized in the same way.

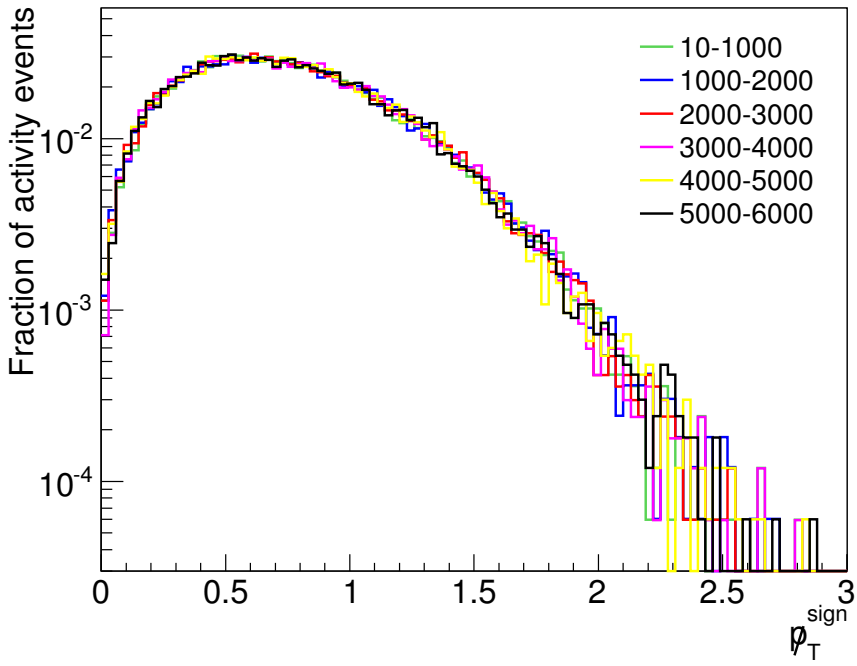

Figure 3.2: Probability distribution of $\not{p}_{\mathrm{T}}^{\mathrm{sign}}$ for six activity bins in MC simulation.

plemented mechanism, which would generate the missing transverse momentum of the simulated collisions. As it turns out, this $\not{p}_{\mathrm{T}}$ stems from finite statistics of particles we are dealing with.

In order to understand this, imagine the transverse plane of the detector as a circle. Let us now generate N_{p} particles with uniformly distributed ϕ and divide the transverse plane in two halves, each spanning π in azimuth (for example, the upper half of the detector $\phi \in (0, \pi)$ and the bottom half $\phi \in (\pi, 2\pi)$). Say that the number of particles with azimuthal angle belonging to the upper half of the detector is N, and number of the remaining particles (those hitting the bottom half) is M (obviously, $M + N = N_{\mathrm{p}}$).

The overall $\not{p}_{\mathrm{T}}$ can be approximated using the mean particle transverse momentum $\langle p_{\mathrm{T}} \rangle$:

$$\not{p}_{\mathrm{T}} \approx \langle p_{\mathrm{T}} \rangle M - \langle p_{\mathrm{T}} \rangle N = \langle p_{\mathrm{T}} \rangle (M - N). \tag{3.9}$$

The uncertainty of this quantity can be evaluated as the error of the indirect measurement:

$$(\delta \not{p}_{\mathrm{T}})^2 = \left(\frac{\partial \not{p}_{\mathrm{T}}}{\partial M} \right)^2 (\delta M)^2 + \left(\frac{\partial \not{p}_{\mathrm{T}}}{\partial N} \right)^2 (\delta N)^2 = \langle p_{\mathrm{T}} \rangle^2 (M + N), \tag{3.10}$$

where δM and δN are the uncertainties of M and N, respectively. The last equality follows from the fact that the standard deviation of the Poisson process is the square root of the number of entries.

One can see that the error of the measurement of missing p_{T} is proportional

to the square root of p_{T} sum:

$$\langle p_{\mathrm{T}} \rangle \sqrt{M+N} \sim \sqrt{\sum_i p_{\mathrm{T},i}}. \tag{3.11}$$

Hence, the significance of the missing p_{T} is, according to the Equations (3.8) and (3.11), missing p_{T} scaled by its error, which is the reason why we see the scaling in Fig. 3.2 and which also confirms the explanation of the origin of the missing p_{T} in our toy MC: $\not{p}_{\mathrm{T}}$ stems from finite statistics of particles we are dealing with.

For the purpose of this Monte Carlo simulation the collision centrality was defined according to the number of produced particles, because we had no other way to comprehend the activity of an event. The experimental particle physics however, offers us numerous tools to measure this quantity. In the following section, the rigorous definition of the collision centrality will be given, as well as the method of its determination.

3.2 Minimum Bias data analysis

In this thesis, two data samples have been analyzed. One of them is minimum bias event sample, which will be discussed in this section. This bulk of the data was selected using the Minimum Bias Trigger Scintillator (MBTS) detectors. These detectors are positioned 3.6 m from the nominal interaction point and provide the full coverage of the azimuthal angle ϕ in the region of pseudorapidity $2.09 < |\eta| < 3.84$. They are divided into eight ϕ and two η sectors, allowing for 16 possible hits per detector side [29]. In addition to this data sample, a jet data sample was used and will be thoroughly analyzed in Section 3.3.

In order to select a pure data sample of inelastic hadronic collisions, several offline selections had to be applied to the triggered event sample. Minimum bias events are required to have at least one existing reconstructed primary vertex (derived from the reconstructed tracks in the ID). Additionally, the time difference between the two MBTS detectors is chosen to be less than 7 ns to efficiently reject beam-halo events. Furthermore, to veto beam-gas events (when an accelerated heavy-ion strikes a residual gas molecule), a coincidence of signals at MBTS and Zero Degree calorimeter was required.

The total integrated luminosity corresponding to this data sample is approximately 0.7 $\mu\mathrm{b}^{-1}$.

3.2.1 Centrality definition and determination

Since the colliding nuclei are extended objects with non-zero volume, the size of the interacting region depends on the impact parameter b of the collision. This physical quantity is defined as the distance between the centers of the colliding nuclei in a transverse plane (see Fig. 3.3). Because it is impossible to directly

measure the value of b [30], physicists introduced the concept of the centrality of the collision, which is directly related to the impact parameter of the collision.

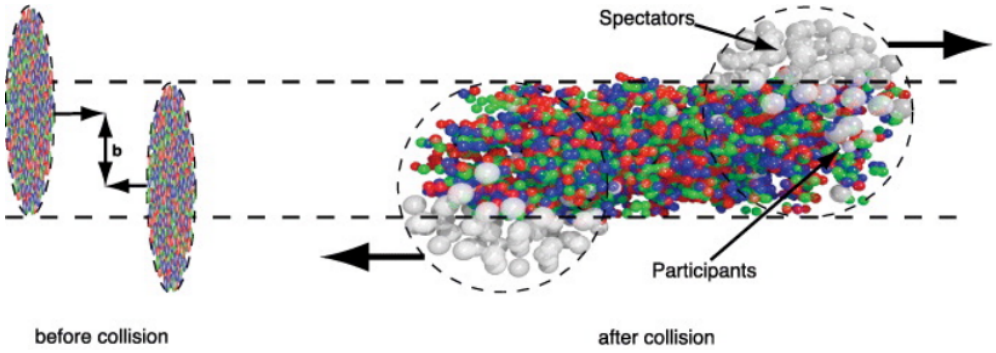

Figure 3.3: Left: the two heavy ions before the collision with the impact parameter b. Right: the spectators remain unaffected while in the participant zone, particle production takes place. Picture adapted from [31].

The collision centrality can be intuitively thought of as the degree of overlap of the two colliding nuclei. It is one of the most important factors in heavy-ion physics, because the system produced in the most overlapping heavy-ion collisions is expected to create the best conditions necessary for QGP production. In other words, closer the collision is to "head-on" (we say the collision is more "central"), the more likely plasma production will be. On the other hand, more "peripheral" collisions are less likely to create ideal conditions for the plasma production [30].

The geometrical Glauber model of multiple collisions [32] treats a nuclear collision as a superposition of binary nucleon-nucleon interactions. The variables used to quantify the collision centrality in this model include the number of participant nucleons N_{part} (that is the number of nucleons that undergo at least one collision) and the number of all nucleon-nucleon collisions N_{coll}. Assuming that nucleons follow straight trajectories we can calculate these quantities for a given value of the impact parameter. While these geometrical quantities are, together with the impact parameter, unobservable, previous studies at RHIC and SPS have shown that the multiplicity and total transverse energy E_{T} are strongly correlated with N_{part}. Multiplicity or total E_{T} are, therefore, used to quantify the centrality in an experiment.

In ATLAS, the PbPb collision centrality is characterized using the summed transverse energy ($\sum E_{\mathrm{T}}$) deposited in the forward calorimeters (FCal). The minimum bias FCal $\sum E_{\mathrm{T}}$ distribution of the data analyzed in this work is illustrated on Fig. 3.4. The FCal $\sum E_{\mathrm{T}}$ is used for this analysis to avoid biasing the centrality measurements by jets, which are produced with the highest probability in the barrel region [18].

It is appropriate to mention that the FCal $\sum E_{\mathrm{T}}$ shown in Fig. 3.4 is not precisely equal to the transverse energy deposited in forward calorimeters. It is

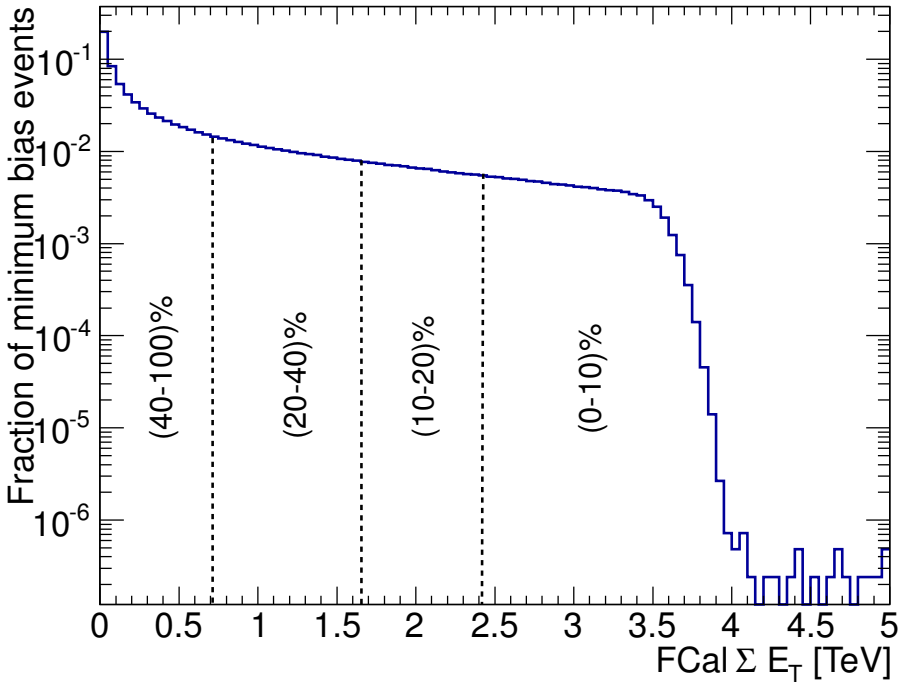

Figure 3.4: Probability distribution of $\sum E_{\mathrm{T}}$ in the forward calorimeters for minimum bias data. The four regions of centrality are indicated by dashed lines and labeled according to increasing fraction of lead-lead total cross section.

slightly modified by applying a necessary calibration factor[4] [33]:

$$\mathrm{FCal}\sum E_{\mathrm{T}}\ (\mathrm{corrected}) = 1.041 \cdot \mathrm{FCal}\sum E_{\mathrm{T}}\ (\mathrm{real}). \tag{3.12}$$

The shape of the energy distribution (Fig. 3.4) can be explained very intuitively. The more frequent peripheral collisions with large impact parameter produce only few particles, which generate only a small response in FCal (the left end of the distribution), while the rare central collisions with small impact parameter generate many more particles because of the increased number of nucleon-nucleon interactions (the right end of the distribution).

For the purpose of this analysis, the fine-grained bins on Fig. 3.4 were combined into 10 larger bins, which are defined according to fractions of the total PbPb cross section in minimum bias events. These bins are expressed in terms of percentiles. By convention, the $(0-10)\%$ bin represents the 10% most central events (highest values of FCal $\sum E_{\mathrm{T}}$) and increasing percentiles refer to events with successively lower FCal $\sum E_{\mathrm{T}}$. The Table 3.1 contains values of FCal $\sum E_{\mathrm{T}}$, which determine different centrality bins, together with the mean values $\langle \mathrm{FCal}\ \sum E_{\mathrm{T}} \rangle$ [33].

Figure 3.5 confirms the assumption that various centrality bins contain, by definition, the same amount of minimum bias events.

[4]Note that in this text, every time we refer to the FCal $\sum E_{\mathrm{T}}$, we mean the corrected value.

Centrality	FCal $\sum E_{\mathrm{T}}$ range [TeV]	$\langle$FCal $\sum E_{\mathrm{T}}\rangle$ [TeV]
$(0-10)\%$	> 2.423	2.903
$(10-20)\%$	$2.423 - 1.661$	2.033
$(20-30)\%$	$1.661 - 1.116$	1.363
$(30-40)\%$	$1.116 - 0.716$	0.885
$(40-50)\%$	$0.716 - 0.430$	0.545
$(50-60)\%$	$0.430 - 0.239$	0.308
$(60-70)\%$	$0.239 - 0.119$	0.160
$(70-80)\%$	$0.119 - 0.053$	0.077
$(80-90)\%$	$0.053 - 0.019$	0.032
$(90-100)\%$	< 0.019	-

Table 3.1: Values of FCal $\sum E_{\mathrm{T}}$ and $\langle$FCal $\sum E_{\mathrm{T}}\rangle$ for the centrality bins used in this analysis.

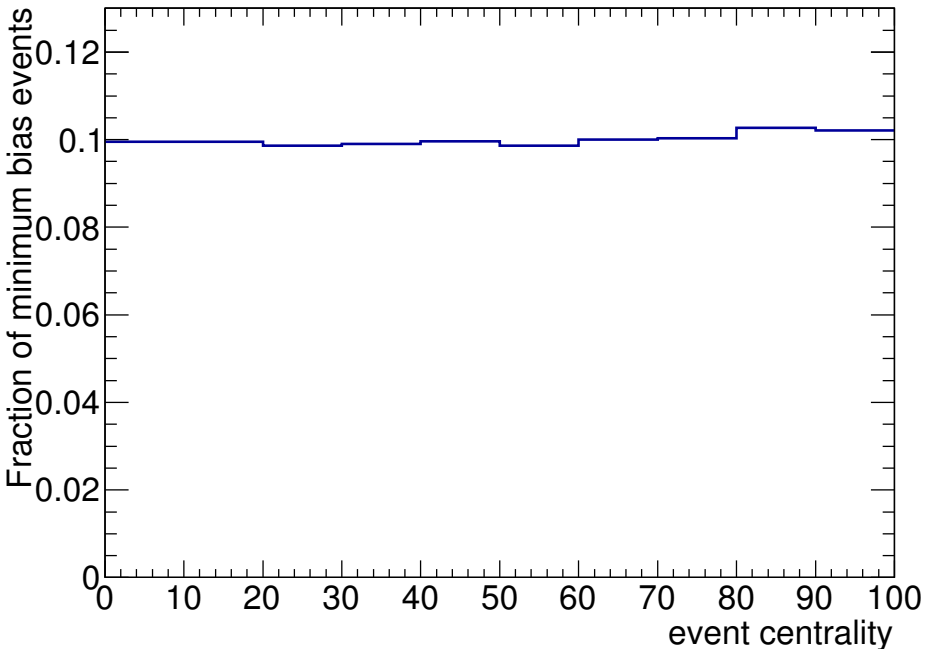

Figure 3.5: Distribution of the fraction of events in 10 centrality bins. The centrality-bin labels run from 0% (most central events) to 100% (most peripheral events).

3.2.2 Corrections for the components of $\not{p}_{\mathrm{T}}$

To investigate the basic behavior of $\not{p}_{\mathrm{T}}$, similar analysis to the one presented in Section 3.1.1 has been made on minimum bias data. The distributions of $\not{p}_{\mathrm{T}}$ and $\not{p}_{\mathrm{T}}^{\mathrm{sign}}$ for centrality bins defined in the previous section are shown in Figures 3.6 and 3.7. The $(90-100)\%$ centrality bin is omitted, because it comprises only the most peripheral collisions, which are not of much interest.

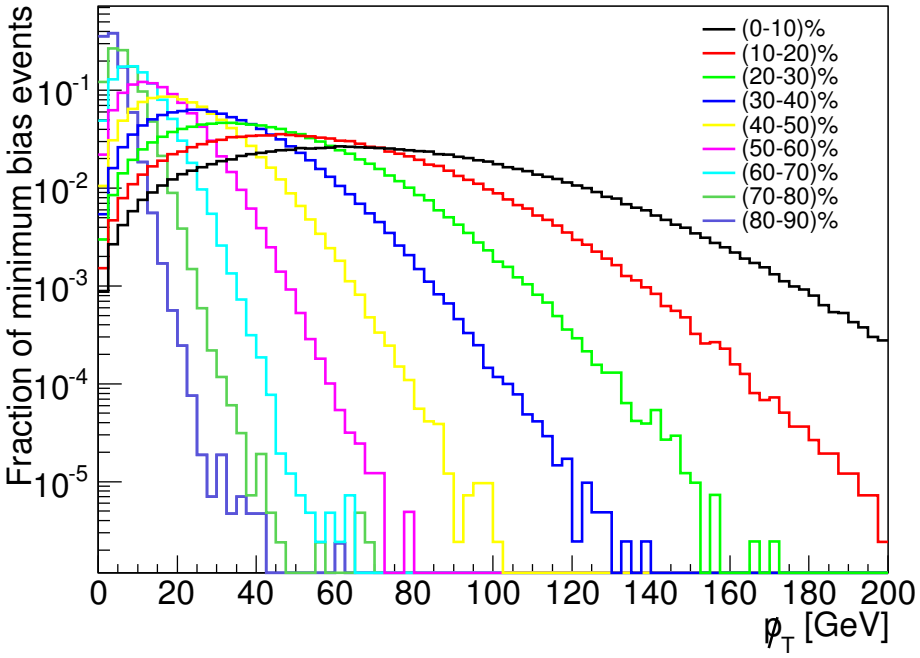

Figure 3.6: Probability distribution of $\not{p}_{\mathrm{T}}$ for nine centrality bins.

As we can observe, the qualitative behavior of the missing transverse momentum is almost identical to the one in Fig. 3.1. However, in comparison to the Fig. 3.2, probability distributions of $\not{p}_{\mathrm{T}}^{\mathrm{sign}}$ for individual centrality bins are not equivalent. This is caused by the malfunctioning regions in ID, which distort the missing p_{T}, as will be shown in the following text.

As already mentioned, some of the missing p_{T} may be generated due to the presence of faults in ATLAS ID system. We shall demonstrate this effect on a simple example. For the sake of simplicity, let us consider the extreme case where one half of the Inner Detector is completely dysfunctional, for example all of the detectors in the range of $\phi \in (0, \pi)$ (that is, the upper half of the detector). If we were now to measure transverse momenta of a huge amount of particles, the overall $\not{p}_{\mathrm{T}}$ would be pointing upwards (towards the faulty parts of the Inner Detector), because no particles have been detected in the range $\phi \in (0, \pi)$.

It is therefore useful to create the "map" of the detector, which would display the faulty spots in the tracking system. It can be done by plotting the density of tracks in two dimensional $\eta \times \phi$ space. This is illustrated on Fig. 3.8.

The natural segmentation in pseudorapidity η does not concern us, since this quantity does not appear in equations mentioned in Section 3.1. The inhomo-

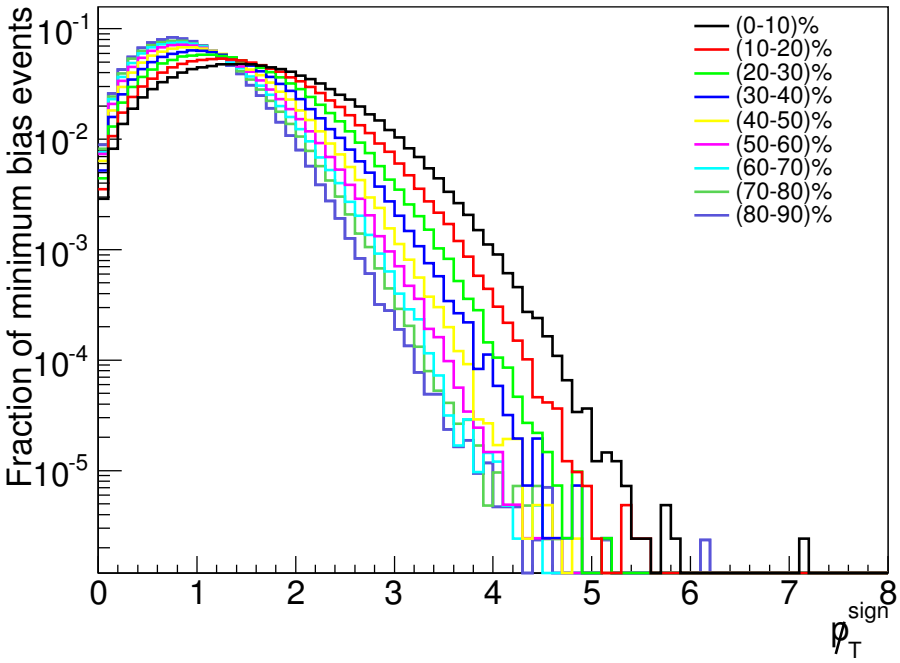

Figure 3.7: Probability distribution of $\not{p}_{\mathrm{T}}^{\mathrm{sign}}$ for nine centrality bins.

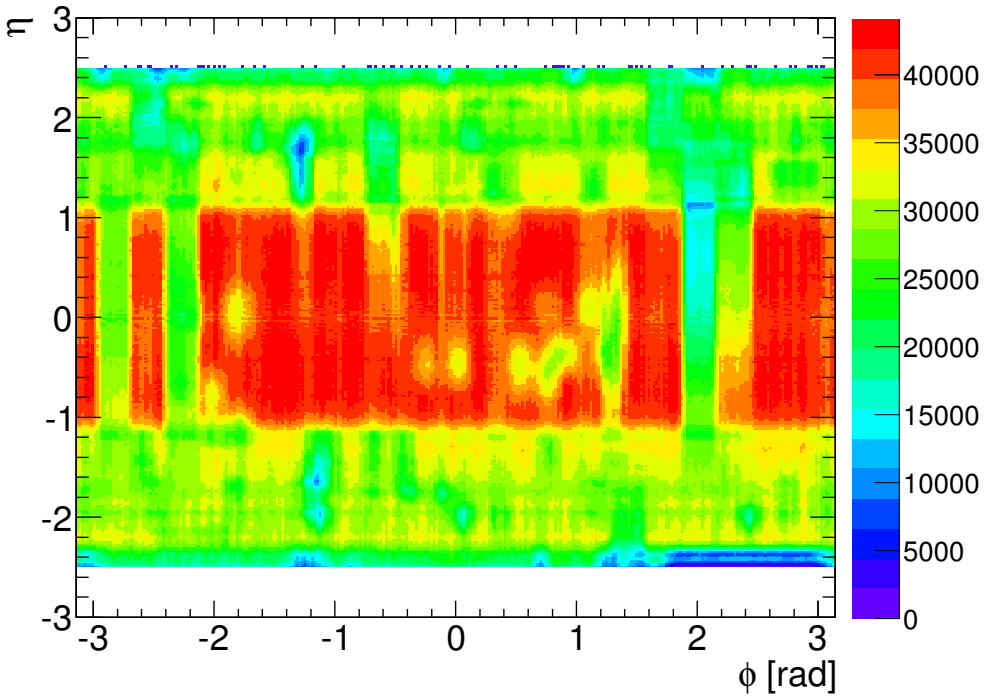

Figure 3.8: Scatter plot illustrating the number of tracks in $\eta \times \phi$ phase space. Color indicates the density of the tracks and is given in numbers, representing the amount of tracks in 0.2×0.2 bins of $\eta \times \phi$ space.

geneity in ϕ, however, has a huge impact on this analysis, because it distorts the calculations of $p^{\mathrm{x}}_{\mathrm{T},i}$ and $p^{\mathrm{y}}_{\mathrm{T},i}$, which are used in Eq. (3.5).

The consequences can be observed in Figures 3.9 and 3.10, where the means of the distributions of x and y components of $\not{p}_{\mathrm{T}}$ are strongly shifted and centrality dependent, while in reality these distributions should be zero-centered. To restore expected centering at zero of these distributions, some corrections for the components of $\not{p}_{\mathrm{T}}$ have to be applied. If we were, for example, able to find the relationships between the means of these distributions and overall FCal $\sum E_{\mathrm{T}}$, we could use them to compensate for the distortions caused by faulty parts of the ID system.

Note that like in the following figures, also in the rest of this work the analyses shall be done for four individual p_{T} ranges: $(0.5-\infty)$ GeV/c, $(0.5-2)$ GeV/c, $(2-4)$ GeV/c, $(4-\infty)$ GeV/c.

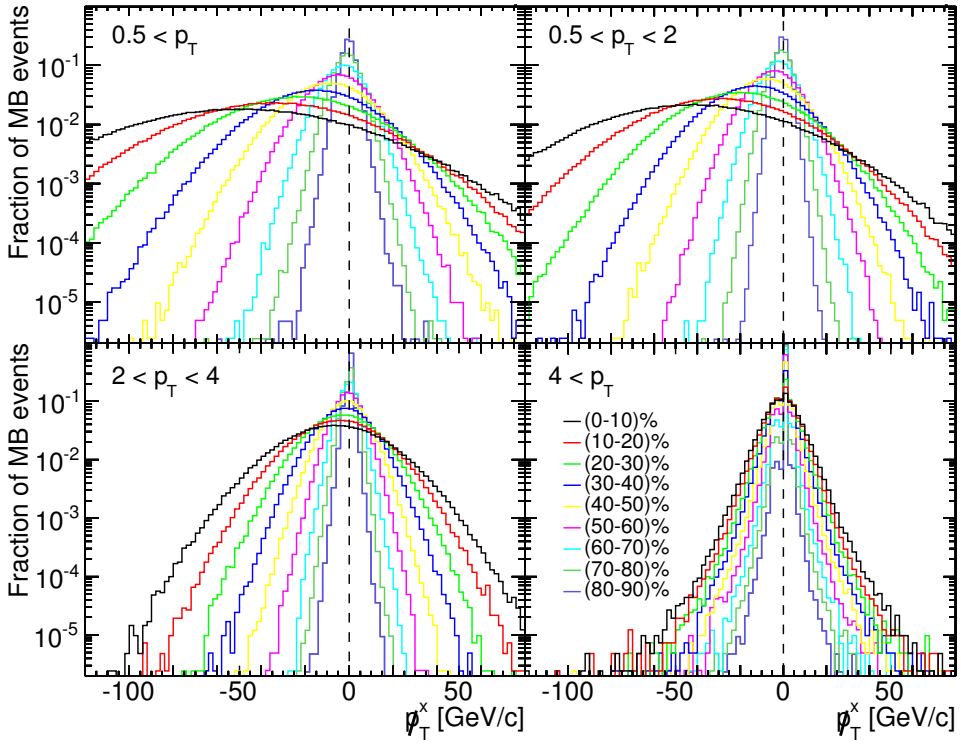

Figure 3.9: Probability distributions of the x component of $\not{p}_{\mathrm{T}}$ for four individual p_{T} bins.

In order to find these relationships, graphs displaying the means of distributions of x ($\langle \not{p}^{\mathrm{x}}_{\mathrm{T}} \rangle$) and y ($\langle \not{p}^{\mathrm{x}}_{\mathrm{T}} \rangle$) components of the overall missing transverse momentum vector as a function of mean FCal $\sum E_{\mathrm{T}}$ ($\langle \mathrm{FCal} \sum E_{\mathrm{T}} \rangle$ (see Table 3.1) have been made. These were fitted using a second order polynomial of the form:

$$\langle \not{p}^{(\mathrm{x,y})}_{\mathrm{T}} \rangle \left(\langle \mathrm{FCal} \sum E_{\mathrm{T}} \rangle \right) = a \cdot \left(\langle \mathrm{FCal} \sum E_{\mathrm{T}} \rangle \right)^2 + b \cdot \langle \mathrm{FCal} \sum E_{\mathrm{T}} \rangle + c, \quad (3.13)$$

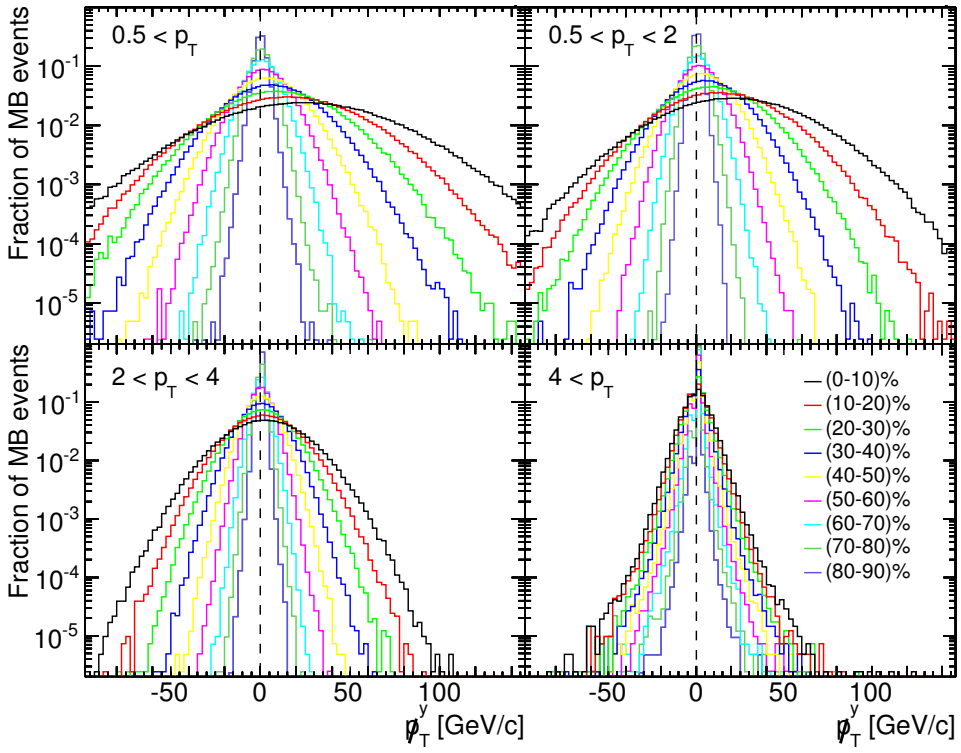

Figure 3.10: Probability distributions of the y component of $\not{p}_{\mathrm{T}}$ for four individual p_{T} bins.

where a,b and c are parameters of the regression[5].

Graphs, along with the fitted functions, are shown in Figures 3.11 and 3.12. The values of the parameters of regressions, estimated in ROOT using the method of least squares, are summarized in Table 3.2.

	$\not{p}_{\mathrm{T}}^{\mathrm{x}}$		$\not{p}_{\mathrm{T}}^{\mathrm{y}}$	
p_{T} range [GeV/c]	a	b	a	b
$0.5 < p_{\mathrm{T}}$	0.69 ± 0.01	-18	0.6	6.6
$0.5 < p_{\mathrm{T}} < 2$	0.27 ± 0.01	-15	0.58 ± 0.01	5.6
$2 < p_{\mathrm{T}} < 4$	-0.086 ± 0.003	-2	0.033 ± 0.003	0.89 ± 0.01
$4 < p_{\mathrm{T}}$	0.031 ± 0.001	-0.25	-0.015 ± 0.001	0.12

Table 3.2: Values of the regression parameters computed in ROOT software. If the values of the parameter and associated error differ by more than two orders of magnitude, the error is not mentioned.

We are now able to use these relations to apply the corrections for the x and y components of missing $\mathbf{p}_{\mathrm{T}}$ such that the means of their distributions will be zero. This can be done by simply taking $\not{p}_{\mathrm{T}}^{\mathrm{x}}$ and $\not{p}_{\mathrm{T}}^{\mathrm{y}}$, and subtracting the value

[5]Note that the value of c was set to zero, since we require the polynomials to go through the origin.

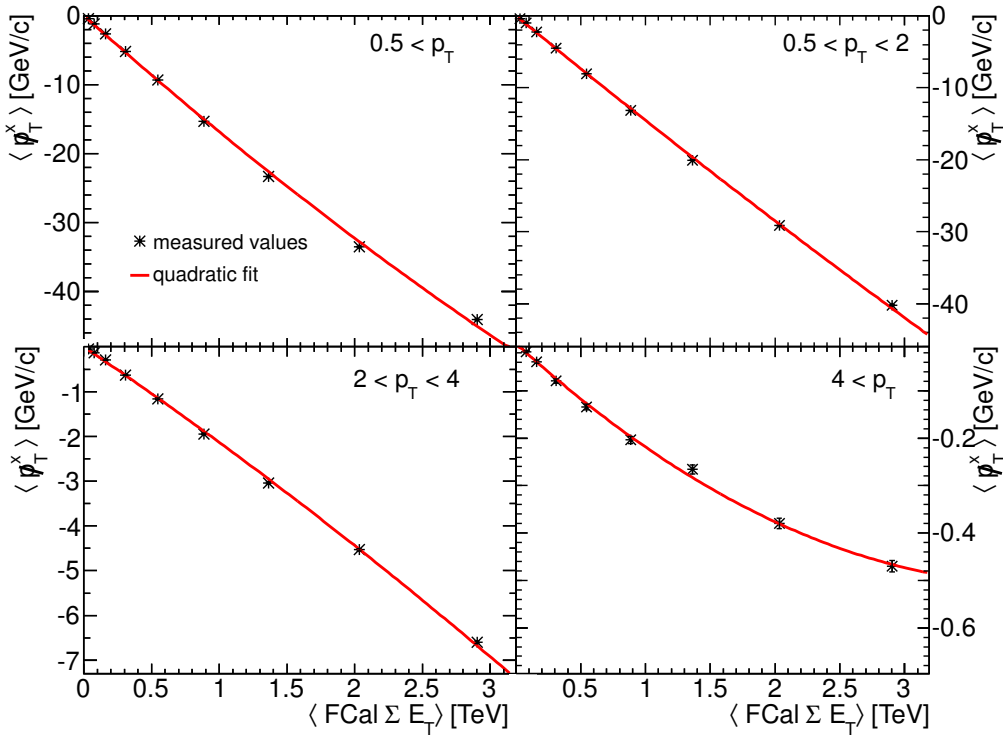

Figure 3.11: The centrality dependence of the average missing transverse momentum in the x direction for four individual p_{T} ranges.

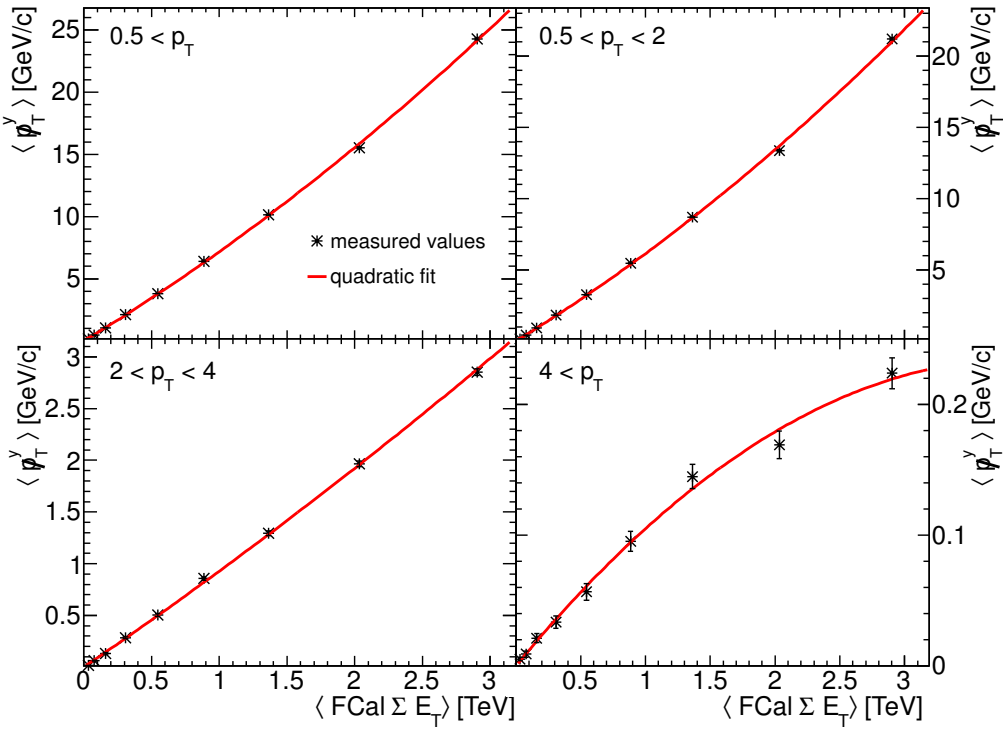

Figure 3.12: The centrality dependence of the average missing transverse momentum in the y direction for four individual p_{T} ranges.

of a corresponding polynomial. For example, let us consider an event, which left a response in FCal with the magnitude of $\overline{\text{FCal } \sum E_{\text{T}}}$. Particles detected by the tracking system are divided into four bins according to their p_{T}. For every one of these bins we calculate the $\not{p}_{\text{T}}^{\text{x}}$ and $\not{p}_{\text{T}}^{\text{y}}$. If we now want to calculate the corrected values of these components $\not{p}_{\text{T}}^{\text{x,corr}}$ and $\not{p}_{\text{T}}^{\text{y,corr}}$, we have to subtract the value of the appropriate polynomial (belonging to the desired component of $\not{\boldsymbol{p}}_{\text{T}}$ and desired p_{T} range) at point $\overline{\text{FCal } \sum E_{\text{T}}}$. In mathematical notation:

$$\not{p}_{\text{T}}^{\text{(x,y),corr}} = \not{p}_{\text{T}}^{\text{(x,y)}} - \left(a \cdot \left(\overline{\text{FCal } \sum E_{\text{T}}} \right)^2 + b \cdot \overline{\text{FCal } \sum E_{\text{T}}} \right), \tag{3.14}$$

where a and b are the values of the parameters taken from Table 3.2.

The means of the probability distributions of the corrected values of $\not{p}_{\text{T}}^{\text{x,corr}}$ and $\not{p}_{\text{T}}^{\text{y,corr}}$ are now really located at $\not{p}_{\text{T}}^{\text{(x,y)}} = 0$ GeV, as clearly seen in Fig. 3.13 and 3.14. In the rest of this work the notation $\not{p}_{\text{T}}^{\text{x}}$ and $\not{p}_{\text{T}}^{\text{y}}$ stands for the corrected values $\not{p}_{\text{T}}^{\text{x,corr}}$ and $\not{p}_{\text{T}}^{\text{y,corr}}$, respectively.

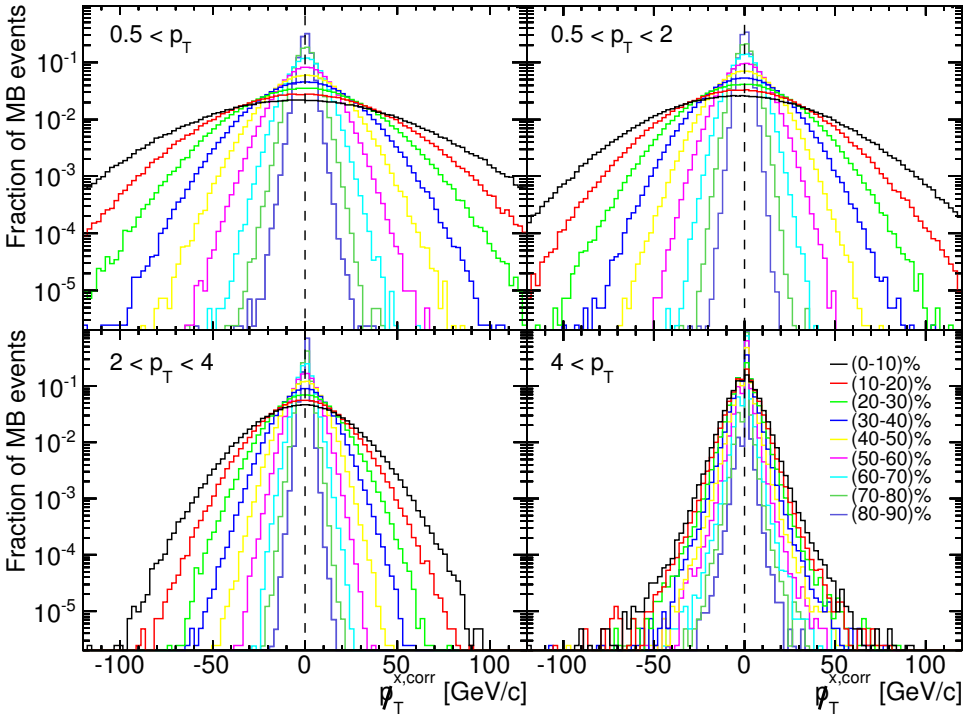

Figure 3.13: Probability distributions of the corrected x component of $\not{\boldsymbol{p}}_{\text{T}}$ for four individual p_{T} ranges.

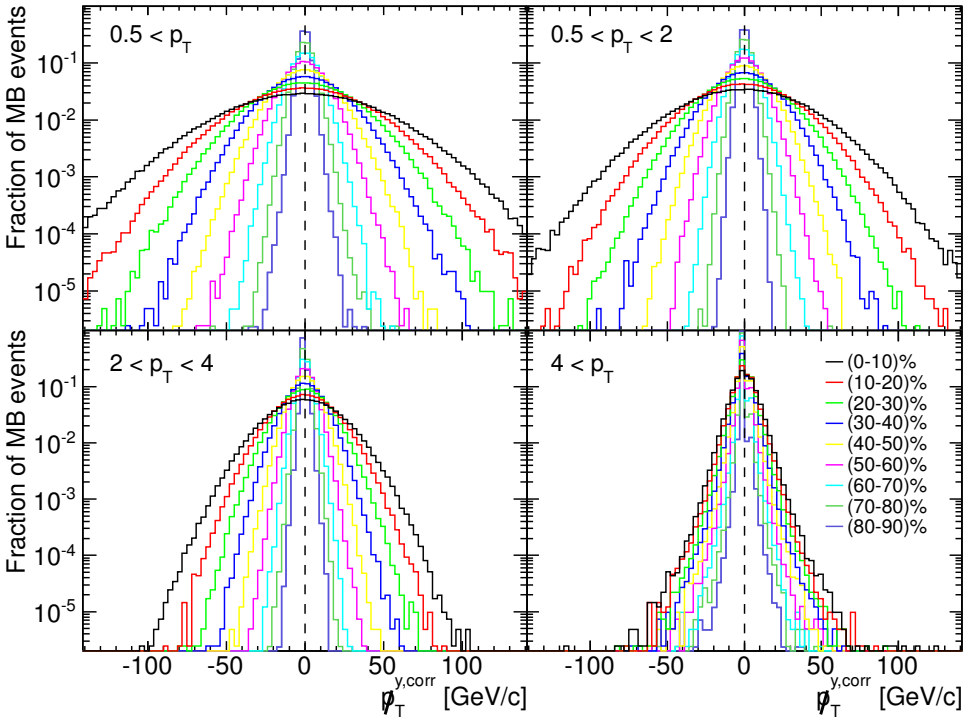

Figure 3.14: Probability distributions of the corrected y component of $\not{p}_{\mathrm{T}}$ for four individual p_{T} ranges.

3.3 Jet data sample

For the purpose of jet analysis, the equally sized centrality bins from previous section were combined into five bins corresponding to the 10% of the most central events (i.e., the most head-on collisions), the next 10% of the events (labeled $(10-20)\%$), and further bins corresponding to the $(20-40)\%$, $(40-60)\%$ and $(60-100)\%$ selections of the total hadronic cross section.

Jets have been reconstructed using the anti-k_t jet clustering algorithm [34] with the radius parameter $R = 0.4$. It is the standard jet algorithm used by both ATLAS [18], and CMS [35]. The transverse energy of the jet is equal to the sum of the transverse energies deposited in calorimeters belonging to the reconstructed jet cone. The average contribution from the underlying event to the jet was subtracted. In order to get results as accurate as possible, efficiency of the ID to reconstruct charge particles had to be taken into account.

The jet data sample corresponds to the total integrated luminosity of approximately 140 $\mu\mathrm{b}^{-1}$.

3.3.1 Event selection

Starting from inelastic hadron collisions based on the selections described in Section 3.2, the basic condition for offline selection of events for the jet analysis is the presence of two jets in the pseudorapidity range of $|\eta| < 2.1$ (to capture

all particles within a jet cone), where the transverse energy of the first (also called leading) jet is required to be $E_{\mathrm{T1}} > 100$ GeV, and the second (subleading) jet is the highest E_{T} jet in the opposite hemisphere with $E_{\mathrm{T2}} > 25$ GeV. In this work, jets are labeled as being in opposite hemispheres if their azimuthal angle separation is $\Delta\phi = |\phi_1 - \phi_2| > \pi/2$. This requirement is used to reduce contributions from multi-jet final states. These settings were adapted from the paper [18].

By selecting leading jets with a rather large transverse energies we ensure high reconstruction efficiency and avoid possible biases caused by inefficiencies close to the trigger threshold. The requirement for the subleading jet assures that this jet is reliably detected above the underlying event.

It is important to characterize the dijet energy balance (or imbalance) with a single quantity. To do so, the jet assymetry ratio, A_J, is introduced:

$$A_J = \frac{E_{\mathrm{T1}} - E_{\mathrm{T2}}}{E_{\mathrm{T1}} + E_{\mathrm{T2}}}, \tag{3.15}$$

where the subscripts 1 and 2 refer to the leading jet and subleading jet, respectively. This construction ensures that A_J is always positive and removes uncertainties caused by possible constant shifts of the jet energy scale. Regular dijet events are expected to have the A_J distribution dominated by the contribution at zero. The deviations from zero are caused by a combination of intrinsic properties of dijets and the jet energy resolution. Energy loss caused by the propagation through the dense medium is expected to produce strong deviations in the reconstructed energy balance. This was indeed observed in [18, 35].

It is important to note that the E_{T2} threshold of 25 GeV constrains the E_{T1}-dependent limit on the magnitude of A_J. For the most common leading jets with energies just above the 100 GeV threshold, this limit is $A_J < 0.6$. The largest possible value of the dijet assymetry ratio for used dataset is $A_J = 0.88$ for the highest energy leading jets with $E_{\mathrm{T1}} \approx 400$ GeV. Jets carrying the energy of this magnitude are, however, very rare, and we can consider $A_J = 0.7$ as an effective upper limit of the energy imbalance.

3.3.2 Overall energy balance of dijet events

Before we present the study of energy imbalance, it is useful to explore the angular behavior of the missing transverse momentum evaluated with respect to the jet position. More precisely, the object of our interest is the angle between the missing momentum vector $\not{\mathbf{p}}_{\mathrm{T}}$ and the axis of leading or subleading jet defined in Section 2.2. Hence, we introduce angular differences α defined as:

$$\alpha_{\mathrm{LJ}} = |\phi_{\mathrm{MPT}} - \phi_{\text{Leading Jet}}|, \tag{3.16}$$

$$\alpha_{\mathrm{SJ}} = |\phi_{\mathrm{MPT}} - \phi_{\text{Subleading Jet}}|, \tag{3.17}$$

where ϕ_{MPT} is the azimuthal angle of $\not{\mathbf{p}}_{\mathrm{T}}$. The behavior of these quantities is shown in Figures 3.15 and 3.16. It is non-trivial, as one can see in the figures.

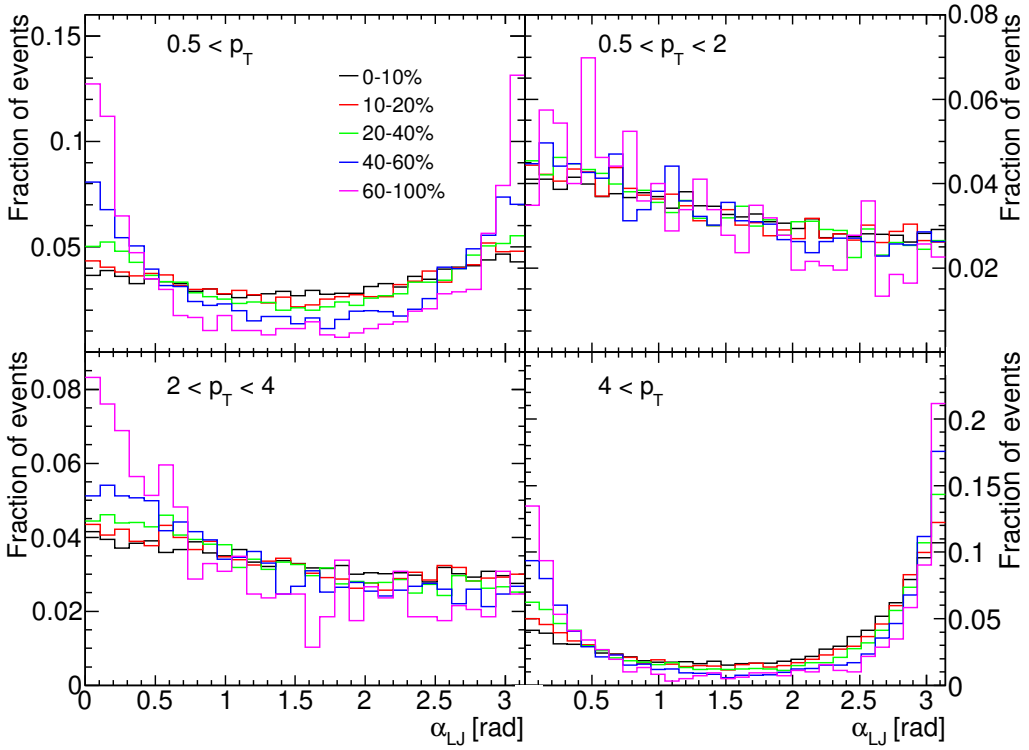

Figure 3.15: Probability distributions of the angle between the $\not{p}_{\mathrm{T}}$ vector and leading jet axis for four individual p_{T} ranges.

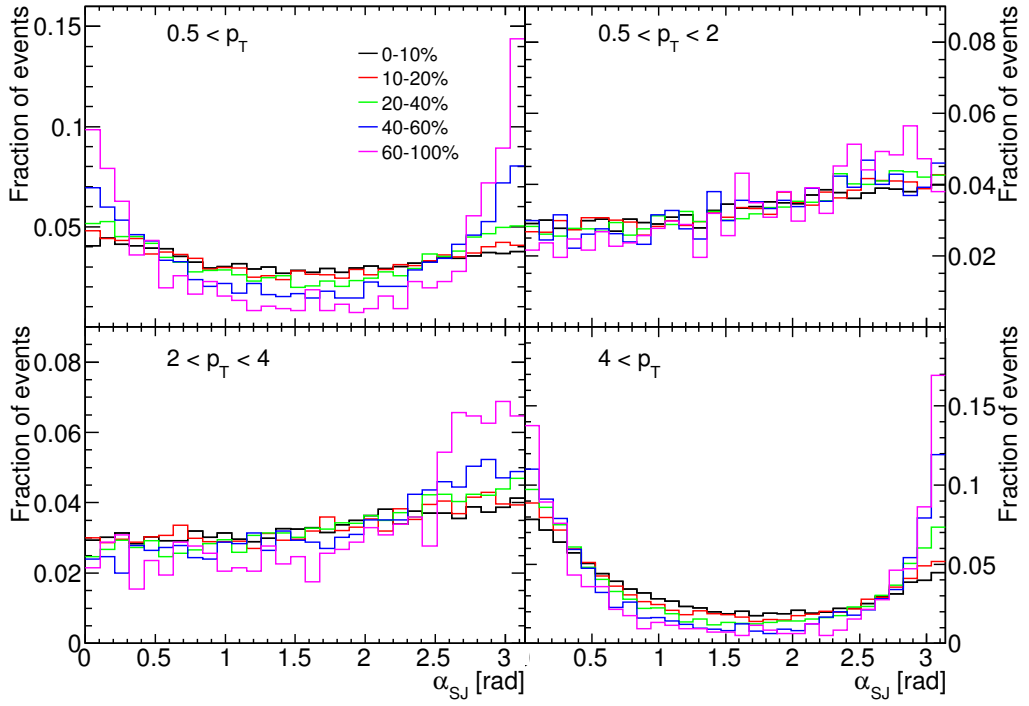

Figure 3.16: Probability distributions of the angle between the $\not{p}_{\mathrm{T}}$ vector and subleading jet axis for four individual p_{T} ranges.

The basic properties seen in the plots are following. For the highest p_{T} particles ($p_{\mathrm{T}} > 4$ GeV/c), we can see that the missing p_{T} points dominantly to the direction of the subleading jet (e.g., α_{LJ} near π in Fig. 3.15), which reflects the fact that the subleading jet has less particles with high-p_{T} than the leading jet. For the lower-p_{T} particles ($0.5 - 4$ GeV/c) the $\not{\boldsymbol{p}}_{\mathrm{T}}$ points dominantly to the leading jet (e.g., α_{LJ} near 0 in Fig. 3.15), which is a consequence of subleading jet having more lower p_{T} particles than the leading jet.

Due to the jet energy resolution effects the leading jet can be misidentified as subleading (and vice versa) and, therefore, we can observe an enhancement of the distributions at zero angles.

It is not easily possible to disentangle the underlying physics from these plots, since jets with different A_J contribute simultaneously to the plots. Moreover, the magnitude of the missing transverse momentum varies in a given centrality bin according to the physics, as we shall further see.

To get some information about the overall energy balance (or imbalance) of dijet events, we can use the projections of $\not{\boldsymbol{p}}_{\mathrm{T}}$ vector of reconstructed tracks onto the axes of both leading, and subleading jets. These were calculated for each event as the scalar projections:

$$\not{p}_{\mathrm{T}}^{||,\mathrm{LJ}} = \not{p}_{\mathrm{T}} \cos \alpha_{\mathrm{LJ}}, \tag{3.18}$$

$$\not{p}_{\mathrm{T}}^{||,\mathrm{SJ}} = \not{p}_{\mathrm{T}} \cos \alpha_{\mathrm{SJ}}, \tag{3.19}$$

where $\not{p}_{\mathrm{T}}$ is the magnitude of the missing transverse momentum vector and α_{LJ} and α_{SJ} are the angles defined in Equations (3.16) and (3.17). Probability distributions of these projections are displayed in Figures 3.17 and 3.18. One can see that the distributions are rather broad, although a clear shift of the mean values can be seen. We can, therefore, average the results over events to obtain the mean values of the projections $\langle \not{p}_{\mathrm{T}}^{||,\mathrm{LJ}} \rangle$ and $\langle \not{p}_{\mathrm{T}}^{||,\mathrm{SJ}} \rangle$. These quantities can be evaluated as a function of centrality and A_J and we shall see that they carry an important physical information.

In Figures 3.19 and 3.20, these average values are shown as a function of event centrality for four track p_{T} bins. Figures 3.21 and 3.22 present the average values of the projections as a function of dijet assymetry ratio, A_J, for two centrality bins, $(0 - 30)\%$ (left) and $(50 - 100)\%$ (right).

These figures show the average missing transverse momentum for tracks with $p_{\mathrm{T}} > 0.5$ GeV/c, projected onto leading and subleading jet axes, as solid black circles. They also show the contributions to the mean $\not{\boldsymbol{p}}_{\mathrm{T}}$ projection for three transverse momentum ranges, displayed as colored bands. For our bulk of data, the main (negative) contribution in Fig 3.19 by the tracks in the $p_{\mathrm{T}} > 4$ GeV/c range is almost perfectly balanced by the positive contributions from the $0.5 - 2$ GeV/c and $2 - 4$ GeV/c regions.

From Fig. 3.19, we can see that with the increasing centrality (centrality going to zero) the size of the $\not{p}_{\mathrm{T}}$ projection calculated using the highest p_{T} particles increases and is negative, which means an excess pointing towards the leading jet

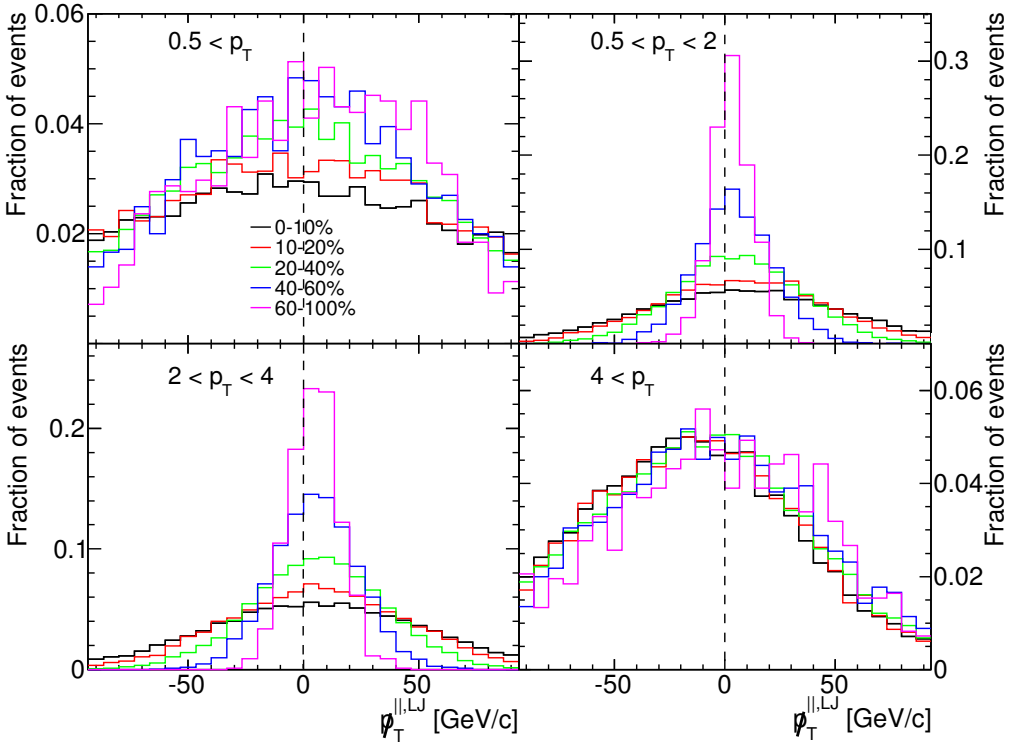

Figure 3.17: Probability distributions of the scalar projection of the $\not{p}_{\mathrm{T}}$ vector on a leading jet axis for four individual p_{T} ranges.

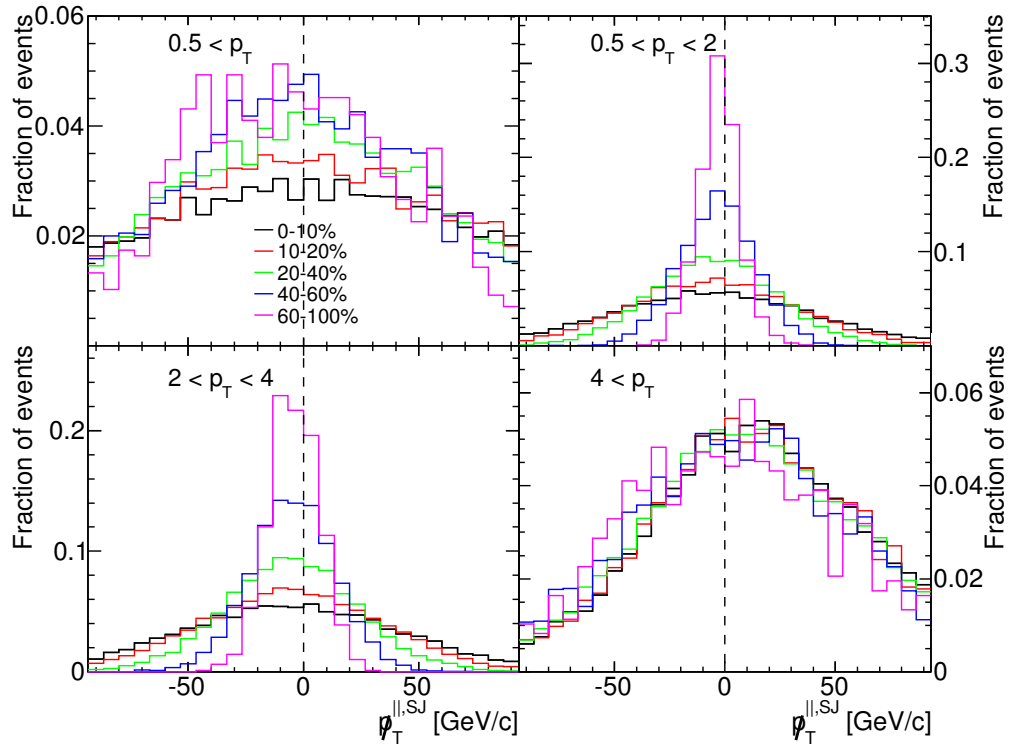

Figure 3.18: Probability distributions of the scalar projection of the $\not{p}_{\mathrm{T}}$ vector on a subleading jet axis for four individual p_{T} ranges.

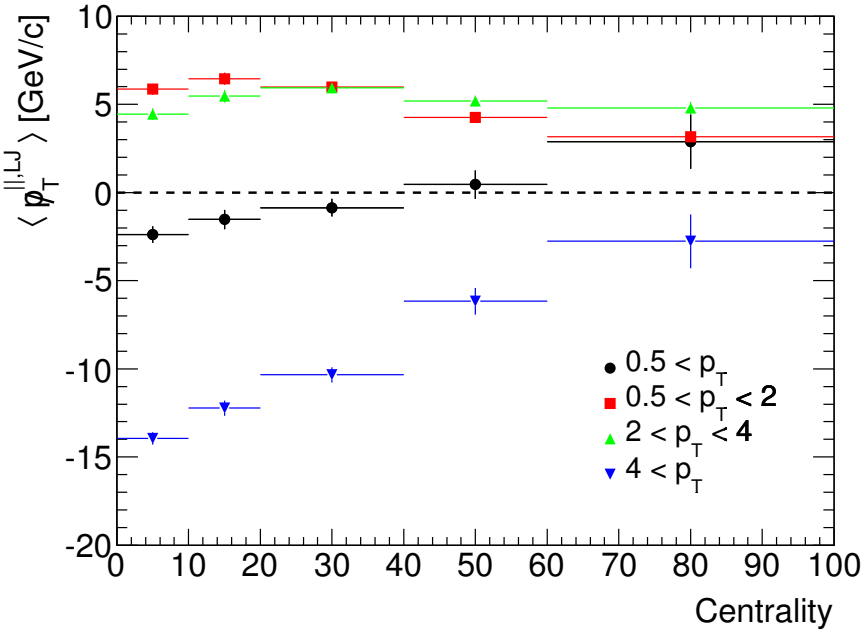

Figure 3.19: Average missing transverse momentum, $\langle \not{p}_{\mathrm{T}}^{||,\mathrm{LJ}} \rangle$, projected onto the leading jet axis for four individual track p_{T} ranges. The $\langle \not{p}_{\mathrm{T}}^{||,\mathrm{LJ}} \rangle$ values are shown as a function of collision centrality. Vertical error bars represent the statistical uncertainties and horizontal represent a size of a given collision centrality bin.

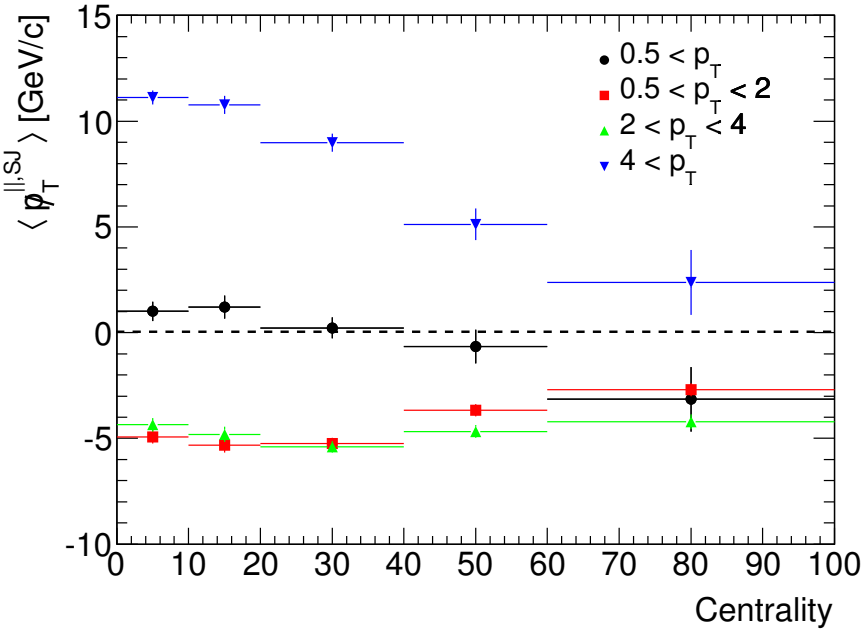

Figure 3.20: Average missing transverse momentum, $\langle \not{p}_{\mathrm{T}}^{||,\mathrm{SJ}} \rangle$, projected onto the subleading jet axis for four individual track p_{T} ranges. The $\langle \not{p}_{\mathrm{T}}^{||,\mathrm{SJ}} \rangle$ values are shown as a function of collision centrality. Vertical error bars represent the statistical uncertainties and horizontal represent a size of a given collision centrality bin.

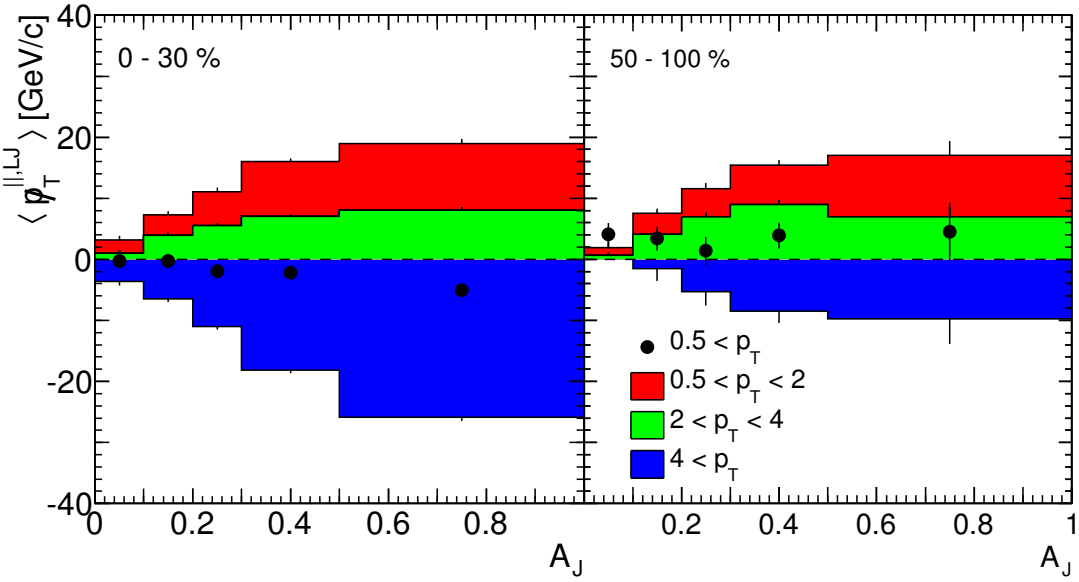

Figure 3.21: Average missing transverse momentum, $\langle p_{\mathrm{T}}^{\parallel,\mathrm{LJ}} \rangle$, projected onto the leading jet axis for four individual track p_{T} ranges. The $\langle p_{\mathrm{T}}^{\parallel,\mathrm{LJ}} \rangle$ values are shown as a function of A_J for $(0-30)\%$ centrality (left) and $(50-100)\%$ centrality (right). The statistical errors are shown as vertical bars.

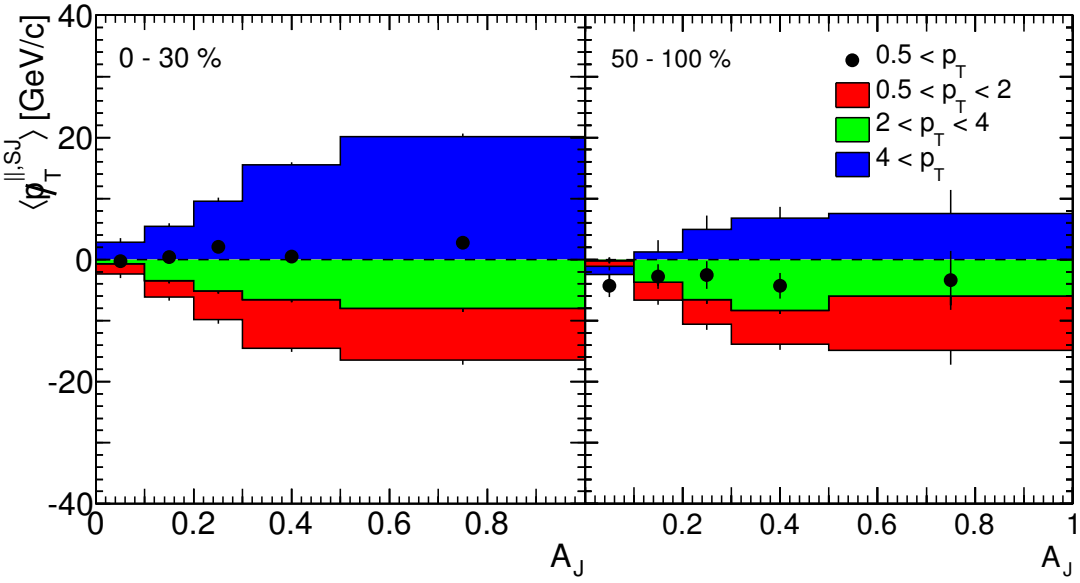

Figure 3.22: Average missing transverse momentum, $\langle p_{\mathrm{T}}^{\parallel,\mathrm{SJ}} \rangle$, projected onto the subleading jet axis for four individual track p_{T} ranges. The $\langle p_{\mathrm{T}}^{\parallel,\mathrm{SJ}} \rangle$ values are shown as a function of A_J for $(0-30)\%$ centrality (left) and $(50-100)\%$ centrality (right). The statistical errors are shown as vertical bars.

($\not{p}_{\mathrm{T}}$ points in the direction of the subleading jet). This means that more hard particles are in the leading jet than in the subleading jet. This excess is compensated by an excess of $\not{p}_{\mathrm{T}}$ calculated using soft particles ($0.5\ \mathrm{GeV/c} < p_{\mathrm{T}} < 2\ \mathrm{GeV/c}$). This means that there is more soft particles in the subleading jet region. The underlying physics picture is following: in central collisions the subleading jet is very often strongly quenched, which means that the yield of hard particles is suppressed. The energy from these hard particles is transferred to soft particles, which show an enhanced yield in central collisions. This physics picture can be concluded also from the plots on Fig. 3.21 and 3.22, which evaluate the mean missing p_{T} projection as a function of dijet asymmetry separately for central (0-30%) and peripheral (50-100%) collisions. With increasing asymmetry the imbalance increases and the lack of the high-p_{T} particles in the subleading jet (negative values of $\not{p}_{\mathrm{T}}^{||,\mathrm{LJ}}$ in Fig. 3.21) is compensated by the excess of soft particles (positive values of $\not{p}_{\mathrm{T}}^{||,\mathrm{LJ}}$ in Fig. 3.21). This effect is stronger for central collisions (left plot) than for peripheral[6] (right plot).

One can also see from these plots that there is relatively good overall balance of the $\not{p}_{\mathrm{T}}$ in the event – the missing p_{T} projection calculated using all particles with $p_{\mathrm{T}} > 0.5$ GeV/c is near zero. This implies that we don't need to go much lower with the minimal p_{T} threshold to capture all the physics.

As expected, the behavior of the average projection onto the subleading jet axis is almost identical to the one for leading jet, only inverted around the line of zero projection (displayed as dashed line in figures). This can be intuitively explained thanks to the fact that most dijet events exhibit back-to-back behavior, which means that the angular difference between the axes of both jets is $\Delta\phi \approx \pi$. This means that the magnitude of the projection of missing transverse momentum on leading jet axis is usually the same as the projection on the subleading jet with the minus sign, and vice versa.

3.3.3 Comparison with the CMS study

These results, especially those displayed in Fig. 3.21, can be compared with the results obtained by CMS detector at LHC, published in [35]. We should note that there are some small differences between their analysis and the analysis in this work. For example, CMS energy requirements for the leading and subleading jets were following: $E_{\mathrm{T1}} > 120$ GeV, $E_{\mathrm{T2}} > 50$ GeV, $\Delta\phi > 2/3\pi$. Moreover, the centrallity bins and track p_{T} ranges are slightly different than those presented in this work.

The main object of our interest are the figures shown in the bottom row of Fig. 3.23. It is possible to directly compare these figures with Fig. 3.21 presented in previous section. As we can see, both of these figures exhibit a very good correspondence between each other. One of the differences, though, are the much smaller statistical uncertainities in our work. This observation can be attributed

[6] (50-100)% are not fully peripheral collisions and some jet quenching is expected to be present also in these collisions.

to the much larger dataset available to our analysis, as opposed to the relatively small sample of data analyzed in [35]. In the CMS study, only a total integrated luminosity of 6.7 μb^{-1} has been included, which is approximately 20 times smaller dataset than the one used in our study.

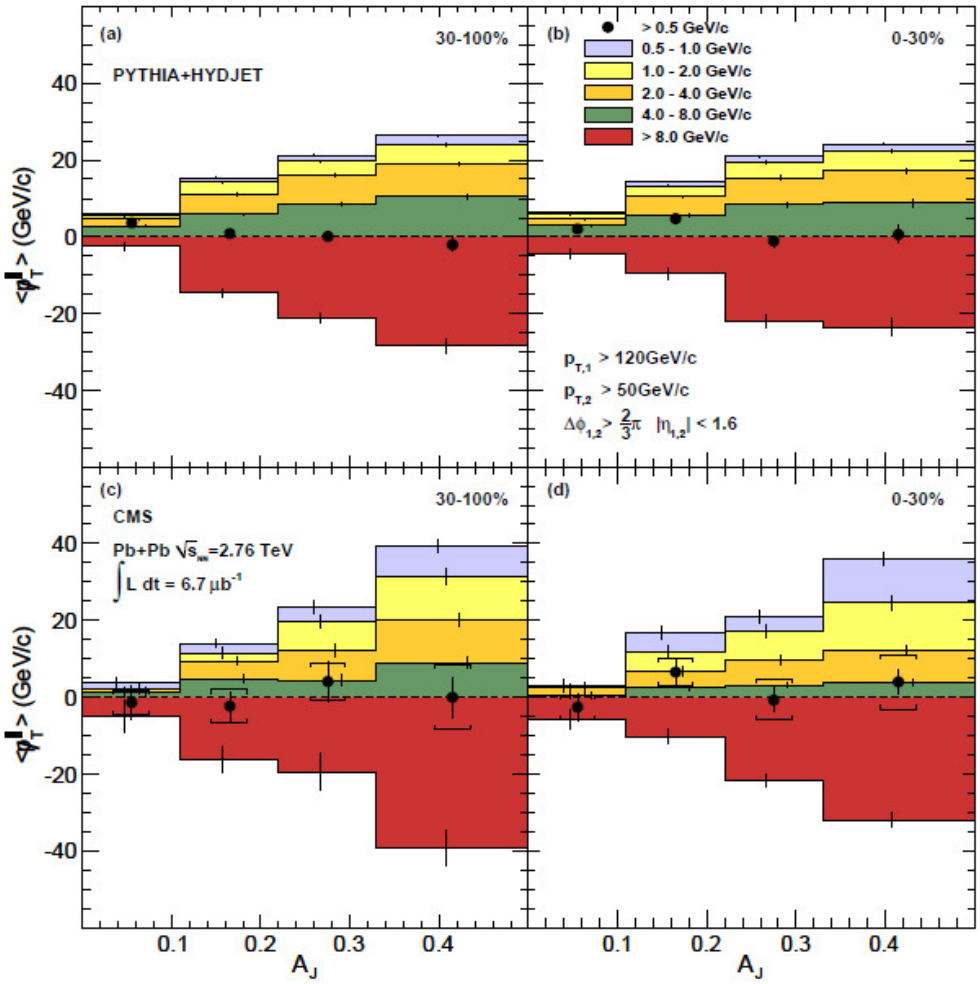

Figure 3.23: Average missing transverse momentum, $\langle \not{p}_{\mathrm{T}}^{\parallel,\mathrm{LJ}} \rangle$, projected onto the leading jet axis for five individual track p_{T} ranges. The $\langle \not{p}_{\mathrm{T}}^{\parallel,\mathrm{LJ}} \rangle$ values as shown as a function of A_J for $(30-100)\%$ centrality (left) and $(0-30)\%$ centrality (right). The statistical errors are shown as vertical bars. The top and bottom rows show results for PYTHIA+HYDJET (MC simulations) and PbPb data, respectively. Figure taken from [35].

Summary and Conclusions

In this work, the data collected by ATLAS detector have been used to investigate the behavior of missing transverse momentum in PbPb collisions at center-of-mass energy $\sqrt{s_{\mathrm{NN}}} = 2.76$ TeV. Before the analysis of the real data a simple MC simulation has been performed to study the basic mechanism of $\not{p}_{\mathrm{T}}$ creation.

We analyzed two main bulks of data. First of them was the minimum bias data sample, corresponding to an integrated luminosity of 0.7 $\mu\mathrm{b}^{-1}$, which has been used to define the collision centrality. These data were also used to construct the corrections for the x and y components of the missing transverse momentum vector. These corrections had to be applied in order to compensate for the faulty parts of the ID tracking system.

The aim of this work was to study the phenomenon of jet quenching and to investigate the relationships between the $\not{\mathbf{p}}_{\mathrm{T}}$ and jets themselves. A jet data sample has been used to elaborate this task. Jets were reconstructed using the anti-k_t jet clustering algorithm with the distance parameter of $R = 0.4$ in a data sample corresponding to an integrated luminosity of 140 $\mu\mathrm{b}^{-1}$. Only events with $|\eta| < 2.1$ having leading and subleading jet energies higher than 100 GeV and 25 GeV, respectively, were selected. Only the tracks with $p_{\mathrm{T}} > 0.5$ GeV/c were used in this study. The p_{T} of tracks was corrected to compensate for the inefficiency of the ID tracking system. The missing transverse momentum projected onto the jet axis has been studied and it has been shown that the overall balance of the transverse momentum can be recovered using tracks with low enough momentum ($p_{\mathrm{T}} > 0.5$ GeV/c). Moreover, a strong increase of yields of highly unbalanced dijets has been shown to be correlated with an increase of production of soft particles associated with the strongly quenched subleading jet.

All things considered, these results provide a critical qualitative and quantitative insight into the transport properties of the medium created in heavy-ion collisions. Furthermore, they are in a very good agreement with previously published results by CMS [35].

Bibliography

[1] K. Yagi, T. Hatsuda, and Y. Miake. *Quark-gluon Plasma.* Cambridge, UK: Cambridge UP, 2005.

[2] M. Munowitz. *Knowing: The Nature of Physical Law.* Oxford: Oxford UP, 2005.

[3] V. Barger, and R. Phillips. *Collider Physics.* Reading, MA: Addison-Wesley Pub., 1997.

[4] D. J. Gross, and F. Wilczek. "Ultraviolet Behavior of Non-Abelian Gauge Theories." *Physical Review Letters* 30.26 (1973).

[5] H. D. Politzer. "Reliable Perturbative Results for Strong Interactions" *Physical Review Letters* 30.26 (1973).

[6] B. Muller. *The physics of the quark-gluon plasma.* Berlin: Springer-Verlag, 1985.

[7] M. G. Alford, et al. "Color superconductivity in dense quark matter." *Reviews of Modern Physics* 80.4 (2008).

[8] M. Stephanov. "QCD Phase Diagram and the Critical Point." *Progress of Theoretical Physics Supplement* 153 (2004).

[9] P. Jacobs, and X. Wang. "Matter in Extremis: Ultrarelativistic Nuclear Collisions at RHIC." *Progress in Particle and Nuclear Physics* 54.2 (2005).

[10] J. D. Bjorken. "Energy loss of energetic partons in quark-gluon plasma: possible extinction of high P(T) jets in hadron - hadron collisions." *FERMILAB-PUB-82-059-THY* (1982).

[11] L. P. Csernai. *Introduction to Relativistic Heavy Ion Collisions.* Chichester: Wiley, 1994.

[12] A. Casher, J. Kogut, and L. Susskind. "Vacuum polarization and the absence of free quarks." *Physical Review D* 10.2 (1974).

[13] Y. L. Dokshitzer, V. A. Khoze, A. H. Mueller, and S. I. Troyan. *Basics of Perturbative QCD.* Atlantica Séguier Frontières, 1991.

[14] "Research." *Mischke QGP-Alice Group.* Web. 08 May 2013. <http://www.staff.science.uu.nl/~misch101/research.htm>.

[15] X. Wang, and M. Gyulassy. "Energy and Centrality Dependence of Rapidity Densities at RHIC Energies." *Physical Review Letters* 86 (2001).

[16] X. Wang. "A pQCD-based approach to parton production and equilibration in high-energy nuclear collisions." *Physics Reports* 280 (1997).

[17] P. Jacobs, and M. van Leeuwen. "High pT in Nuclear Collisions at the SPS, RHIC, and LHC." *Nuclear Physics A* 774 (2006).

[18] G. Aad, et al. (The ATLAS Collaboration) "Observation of a Centrality-Dependent Dijet Asymmetry in Lead-Lead Collisions at $\sqrt{s_{\mathrm{NN}}} = 2.76$ TeV with the ATLAS Detector at the LHC." *Physical Review Letters* 105.25 (2010).

[19] L. Evans, and P. Bryant. "LHC machine." *Journal of Instrumentation* 3.08 (2008).

[20] A. Beuret, et al. "The LHC lead injector chain." *Proceedings of EPAC* (2004).

[21] "CERN Accelerating Science." *CERN Document Server.* 08 May 2013. <http://cds.cern.ch/record/841555/?ln=sk>.

[22] G. Aad, et al. "The ATLAS experiment at the CERN large hadron collider." *Journal of Instrumentation* 3.08 (2008).

[23] "ATLAS Experiment." *ATLAS Experiment.* Web. 31 Mar. 2013. <http://www.atlas.ch/detector.html>.

[24] J. Beringer, et al. "Review of particle physics." *Physical Review D* 86.1 (2012).

[25] A. R. Baden. "Jets and kinematics in hadronic collisions." *International Journal of Modern Physics A* 13.11 (1998).

[26] C. Adler, et al. "Pion Interferometry of $\sqrt{s_{\mathrm{NN}}}$=130 GeV Au+Au Collisions at RHIC." *Physical Review Letters* 87.8 (2001).

[27] A. Gurtu. "Missing transverse energy performance of the CMS detector." *Journal of Instrumentation* 6.9 (2011).

[28] "ROOT | A Data Analysis Framework." *ROOT | A Data Analysis Framework.* Web. 14 Apr. 2013. <http://root.cern.ch/drupal/>.

[29] G. Aad, et al. "Measurement of underlying event characteristics using charged particles in pp collisions at $\sqrt{s}$= 900 GeV and 7 TeV with the ATLAS detector." *Physical Review D* 83.11 (2011).

[30] R. Vogt. *Ultrarelativistic Heavy-ion Collisions.* Amsterdam: Elsevier, 2007.

[31] R. Snellings. "Elliptic flow: a brief review." *New Journal of Physics* 13.5 (2011).

[32] R. J. Glauber. "Quantum Optics and Heavy Ion Physics." *Nuclear Physics A* 774 (2006).

[33] `https://twiki.cern.ch/twiki/bin/viewauth/AtlasProtected/HeavyIonAnalysis2011` (ATLAS internal communication).

[34] M. Cacciari, G. P. Salam, and G. Soyez. "The anti-k_t jet clustering algorithm." *Journal of High Energy Physics* 2008.04 (2008).

[35] S. Chatrchyan, et al. (The CMS Collaboration) "Observation and studies of jet quenching in PbPb collisions at $\sqrt{s_{\mathrm{NN}}} = 2.76$ TeV." *Physical Review C* 84.2 (2011).